Annual Report on Research Activities 2013

Tanabe Photonic Structure Group,

Department of Electronics and Electrical Engineering,

Faculty of Science and Technology, Keio University

Picture of lab members taken at Spring Colluquium Meeting on April 2013

Contents

Foreword

I am very thankful to everyone who is supporting our group, in the Department of Electronics and Electrical Engineering, in Keio University, Japan.

Year 2013 was the third year since we started our research activities in 2011. In March 2014, four master-course students graduated and two of them started their new carrier in industry. Other two students are now in a different department where they are pursuing their sub-major to complete their double master degree. They are research assistants of the Leading Graduate School Program in Keio University, where they will come back to our group next year as a PhD student after they obtained a double master degree.

After three years, our group has grown sufficiently to regard as a research lab, since we now have a number of students and sufficient facilities to do research. Our activities that we started three years ago are now in a level where we can publish as a research paper. For example, the microcavity fabrication with crystal growth has been published in conferences and in journal papers.

We have selected some of our research topics, and put them together to make this report. All of the manuscripts are written by bachelors and master-course students. Therefore, I admit that some sentences are not well written. Even though, I am confident that the scientific contents provide important information and you may find interest in our research activities. I am appreciating and glad if you will give us any feedback to our researches.

August, 2014.

Takasumi Tanabe, Associate Professor,

Department of Electronics and Electrical Engineering,

Keio University

Lab Members (Names and their positions after graduation)

Associate Professor
Takasumi Tanabe

Master 2nd Grade: (The class of 2011)
Yohei Ogawa	Starts his carrier in industry
Takumi Kato	Pursue sub-major master degree in School of Medicine, Keio University
Hiroshi Kudo	Starts his carrier in industry
Wataru Yoshiki	Pursue sub-major master in School of Business & Commerce, Keio Univ.

Master 1st Grade: (The class of 2012)
Ryusuke Saito	Continues his education in the graduate school of Keio University
Ryo Suzuki	Continues his education in the graduate school of Keio University
Tomohiro Tetsumoto	Continues his education in the graduate school of Keio University
Jiro Nishimura	Continues his education in the graduate school of Keio University
Akihiro Fushimi	Continues his education in the graduate school of Keio University

Bachelor 4th Grade: (The class of 2013)
Tomoya Kobatake	Continues his education in the graduate school of Keio University
Sho Tamaki	Continues his education in the graduate school of Keio University
Shohei Tomiyama	Continues his education in the graduate school of Keio University
Zhelum Chen	Continues his education in the graduate school of Keio University
Yosuke Nakagawa	Continues his education in the graduate school of Keio University
Yui Yakushiji	Starts her carrier in industry

Research Activities

Investigation of the loss mechanism in a silica toroid microcavity

Sho Tamaki (B4)   Tomohiro Tetsumoto (M1)   Wataru Yoshiki (M2)

We must obtain a silica toroid microcavity with a high Q factor if we are to generate various nonlinear optical effects. Factors limiting the quality factor of a silica toroid microcavity have been studied theoretically, and the effects of, for example, the impurity of a Si wafer, Rayleigh scattering loss, and the adhesion of water molecules have been analyzed. However, when it comes to an actual measurement, none of these are dominant because the Q limited by these factors becomes dominant when its value exceeds 10^8 but the measured value is usually $Q < 10^7$. Therefore, we investigated other effects limiting the current Q factor of a silica toroid microcavity. We studied the effects of cavity fabrication methods, the external environment, optical measurement, and the cavity structure. As a result of our investigation, we succeeded in achieving $Q = 6.5 \times 10^7$, which is an improvement on the highest Q factor of $Q = 2.0 \times 10^6$ that we reported last year.

Key words : Air cleanliness class, surface roughness, fundamental mode

1. Abstract

The silica toroid microcavity was first described as an attractive platform for studying various optical nonlinear phenomena in 2003 because of its ultra-high Q and because it could be fabricated on a chip [1]. The cavity is fabricated with the following procedure. First, a Si wafer is thermally oxidized and a silica layer is formed. Then a circular pattern is formed photolithographically (details omitted). Next, the Si wafer is etched with reactive gas XeF_2. Finally, a CO_2 laser is irradiated from above (this process is called "reflow"). The procedure is outlined in Fig. 1.
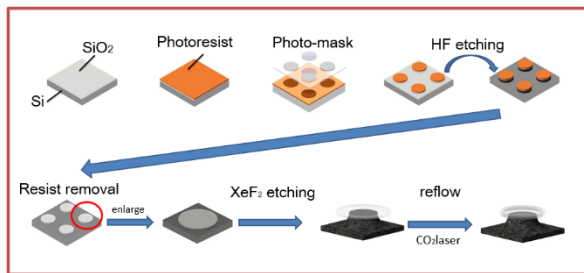

Fig. 1: Fabrication of a silica toroid microcavity.

The performance of the cavity is not limited by the use of photolithography. Therefore, in this study, we investigated to the way in which the Q factor was affected by the reflow process, changes in air cleanness, the profile of the CO_2 laser, the optical measurement method and the cavity structure.

2. Reflow

After XeF_2 etching, a silica disk supported by a Si pillar is irradiated from above by a CO_2 laser and the silica disk forms a toroidal shape. This phenomenon occurs as a result of the difference between the heat absorption coefficients of Si and silica. Since Si has a much higher heat absorption coefficient, when a CO_2 laser is irradiated from above, the heat around the center of the silica disk flows into the Si pillar whereas heat at the edge of the silica disk is concentrated and the silica disk melts. We can expect that one way of obtaining a high Q is to reduce surface roughness. We considered the reflow process to be crucial as regards surface roughness. Therefore, in this study we changed the CO_2 laser irradiation profile in two ways. One involved using pulse irradiation, which is the conventional approach, and the other involved using lamp irradiation.
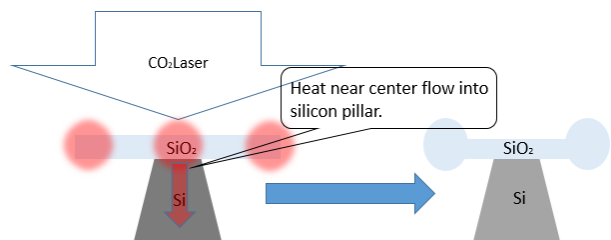

Fig. 2: Reflow process

We found that by changing from pulse to lamp irradiation, the Q factor and the surface roughness both improved from $Q = 3.9 \times 10^6$ to $Q = 1.7 \times 10^7$ and from 181 nm to 4 nm, respectively, as shown in Fig. 3.
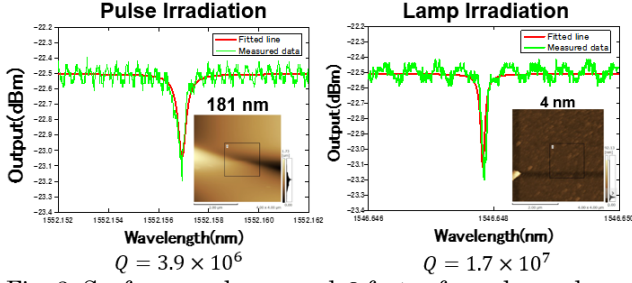
Fig. 3: Surface roughness and Q factor for pulse and lamp irradiation.

3. Optical measurement

In addition to the improvement achieved by fabricating a better cavity, we found that the Q factor can be greatly influenced by optical measurement. The optical model for a toroidal cavity can be expressed as shown in Fig. 4 [2]. When the fundamental mode is excited, the propagation constants in tapered optical fiber and in the cavity have the relationship expressed by eq. (1) below.

$$\beta_{\text{taper}}(a_f) \cong \left[1 - \left(\frac{a - r_e + a_f}{2R_e}\right)\right]\beta_e \qquad (1)$$

β_{taper}: The propagation constant in tapered optical fiber
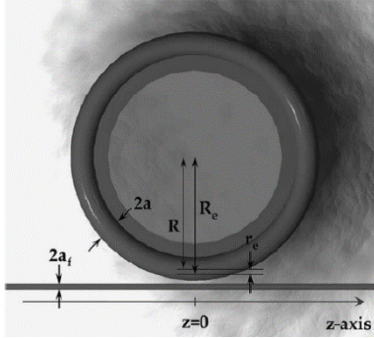β_e: The propagation constant in the cavity

Fig. 4: Optical model of a toroidal cavity.[B. Min, L. Yang, and K. Vahala, "Perturbative analytic theory of an ultrahigh-Q toroidal microcavity," Phy. Rev. A , **76**, 013823, (2007)] [2].

Eq. (1) and Fig. 4 show that $a, r_e. R_e$ and $\beta_e(a)$ are determined by the cavity. Therefore, when the diameter of the tapered fiber is changed, a different mode is excited. The experimental results are shown in Fig. 5.
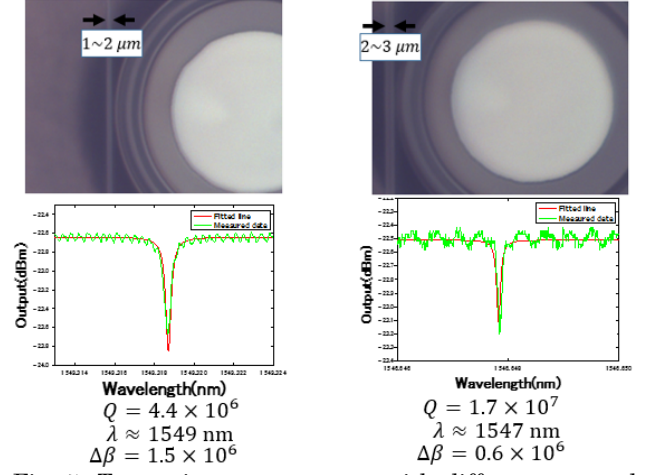

Fig. 5. Transmittance spectrum with different tapered fiber diameters. （$\Delta\beta$ is the value which is briefly calculated difference between the left side and the right side of eq. (1).)

As seen in Fig. 5, we found that by changing the diameter of the tapered fiber, a different mode was excited and the Q factor was greatly improved. The reason for the improvement in the Q factor caused by the different mode is explained in Fig. 6. When the fundamental mode is excited, the light is confined in plane. On the other hand, in a higher order mode, the light is confined in plane and also vertically. Therefore, when light is confined in a higher order mode, it is influenced more by the surface effects than when the fundamental mode is excited.
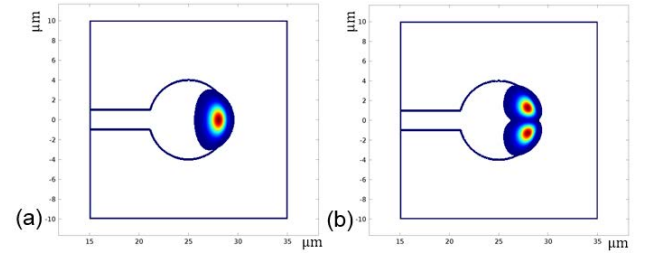
Fig. 6(a): Electrical field of FEM simulation for fundamental mode. (b): Electrical field of FEM simulation for second order mode.

4. External environment

As part this year's improvements, our laboratory was renovated and we created a semi-clean room where the air cleanliness class was improved from 50000 to 5000. This renovation improved the preservation of cavities and we can expect impurity adhesion to be reduced. In this study, we exposed a cavity with a Q factor of $Q < 10^7$ outside the laboratory (air cleanliness class 50000) for about 48 hours and compared the transmittance spectra (shown in Fig. 7) obtained before and after exposure.

Fig. 7: Transmittance spectrum before exposure (left), and after exposure (right).

As shown in Fig. 7, the Q factor decreased almost by half from $Q = 1.4 \times 10^7$ to $Q = 7.0 \times 10^6$. This was because the adhesion of impurities to the cavity caused the surface scattering of 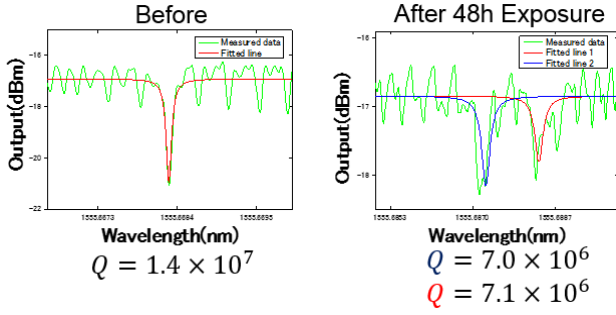light, which is considered loss. Also, the transmittance spectrum had two dips. The origin of this phenomenon is back-scattering light. When light is reflected at a point where impurities adhere, a portion of the light scatters at the surface and constitutes a loss and another portion of the light scatters back and couples back to the cavity. Therefore, we revealed that a conventional environment limited the Q factor to $Q < 10^7$

5. Cavity structure

We have shown the effects of changes in the reflow method, optical measurement and external environment in terms of maximizing the Q factor of a cavity. Next, we changed the diameter of the Si pillar and the minor diameter of the cavity (minor diameter corresponds to a in Fig. 4.) Fig. 8(a) and (b): SEM images of two cavities with different minor diameters and their transmittance spectra.

Fig. 8 (a) and (b) reveal that the Q factor was greatly changed by changing the cavity structure. To investigate the reason for this, we performed an FEM simulation for Fig. 8(a) and Fig. 8(b) as shown in Fig. 9(a) and (b).
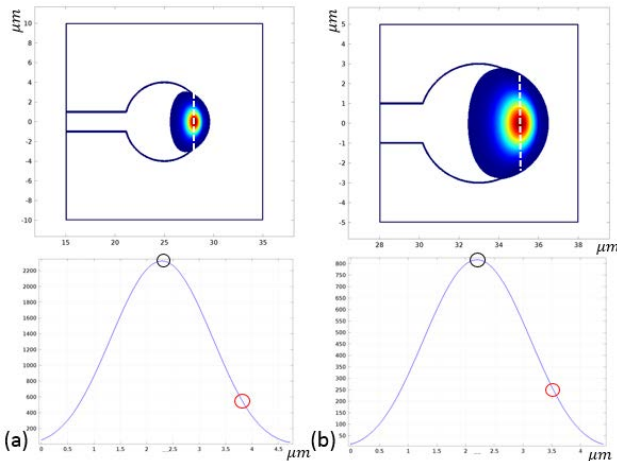

Fig. 9 (a) and (b): Electrical field of FEM simulation and the graph of the intensity of its electrical field in the section shown by a broken white line.

In Fig. 9 (a) and (b), the intensity at the surface divided by the maximum intensity for each cavity was 0.25 and 0.32, respectively. Therefore, in Fig. 8(b), the light was more likely to be influenced by the surface than in Fig. 8(a) and thus exhibited a lower Q factor.

6. Conclusion

In this study, we investigated the effects of changes in reflow, optical measurement, external environment and cavity structure. As a result, we revealed that the conventional reflow method limited the Q factor to $Q < 10^7$, optical measurement limited the Q factor to $Q < 10^7$, a conventional environment limited the Q factor to $Q < 10^7$ and the cavity structure limited the Q factor to $Q < 10^6$. Ultimately, as shown in Fig. 8(a), we achieved a Q factor of $Q = 6.5 \times 10^7$.

Table. 1 Factors limiting Q factor and Q factor limits

Limiting factors	Limits of Q factor
Reflow methods	$Q < 10^7$
Optical measurement	$Q < 10^7$
External environment	$Q < 10^7$
Cavity structure	$Q < 10^6$

References

[1] D.K. Armani, T.J. Kippenberg, S.M. Spillane, and K.J. Vahala, "Ultra-high-Q toroid microcavity on a chip," Nature, vol. **421**, (2003).
[2] B. Min, L. Yang, and K.J. Vahala, "Perturbative analytic theory of an ultrahigh-Q toroidal microcavity," Phy. Rev. A , **76**, 013823, (2007).

Kerr comb generation: analysis and experiment

Takumi Kato(M2)   Ryo Suzuki(M1)

We analyzed optical Kerr comb generation in a microcavity and demonstrated Kerr comb generation experimentally using a silica toroidal microcavity. We calculated Kerr comb using a Lugiato-Lefever model with a split-step Fourier method. We succeeded Kerr comb generation and measured the radio frequency signal to understand the condition of the Kerr comb.

Key word: Optical microcavity, Four wave mixing, Kerr comb, Split-step Fourier method

1. Introduction

A microcavity with an ultra-high quality factor *(Q)* and a small mode volume *(V)* is suitable for applications requiring a nonlinear optical effect, and optical frequency comb generation is one expected application. A microcavity can generate cascade four wave mixing with a small input power. And this wavelength conversion and filtering effect of a microcavity result in optical Kerr comb generation[1]. A Kerr comb is not always in a mode locked condition but in a noisy condition. Recently, how ways of achieving a mode locked condition have been intensively investigated[2][3].

There are two methods for calculating a Kerr comb numerically. One is modal expansion[4] and the other is the split-step Fourier method[5]. In this study, we analyzed a Kerr comb using the split-step Fourier method and clarified the condition that achieves mode locking. We also conducted Kerr comb generation experiments using a silica toroidal microcavity.

2. Numerical analysis of Kerr comb generation

2.1 Theory

We use a generalized mean-field Lugiato-Lefever equation (LLE) to analyze the evolution of a Kerr comb in a microcavity[5][6]. And, we solved it with the split-step Fourier method.

$$t_R \frac{\partial^2 E}{\partial r^2} = \left(-\frac{\alpha}{2} - \frac{\kappa}{2} - i\delta_0 + \frac{iL\beta_2}{2}\frac{\partial^2 E}{\partial t^2} + iL\gamma|E|^2 \right)E + \sqrt{\kappa}S \quad (1)$$

where, $t_R, \alpha, \kappa, \delta_0, L, \beta_2, \gamma$ and S are the round-trip time, intrinsic cavity loss, coupling loss, detuning of the input wavelength, cavity length, second order dispersion of the cavity, nonlinear coefficient, and input driving power, respectively. Since β_2 includes geometrical dispersion, we calculated this parameter with the finite element method(FEM). The nonlinear coefficient is $\gamma = \frac{n_2\omega}{cA_{eff}}$ where $n_2 = 2.2 \times 10^{-20}$ m^{2}W^{-1} is the Kerr nonlinearity of silica. A_{eff} is the effective mode area and can be calculated with FEM. Figure 1 shows the FEM calculation. The material dispersion is calculated by using the Sellmeier equation.

Using these parameters which model a silica toroidal microcavity, we calculated LLE with the split-step Fourier method. One step corresponds to the cavity length.
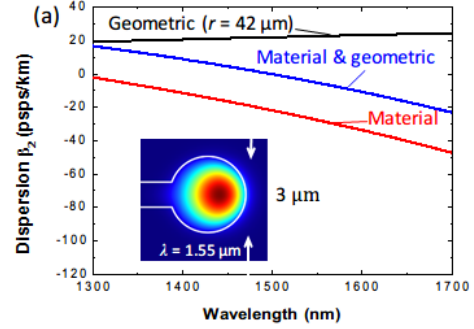

Fig. 1: 2nd order dispersion and mode profile of a silica toroidal microcavity.
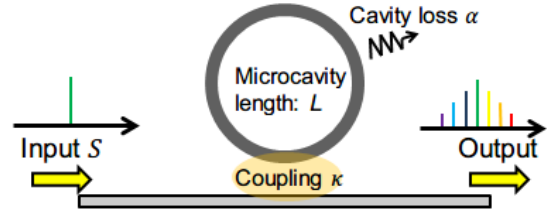

Fig. 2: Schematic image of numerical simulation of an optical Kerr comb in a microcavity.

2.2 Analytical result: soliton formation

We transformed the cavity loss into a Q factor to make it easy to compare between the numerical and experimental results. The relation between cavity loss and Q factor is described as

$$Q = \omega\tau_p = \omega\frac{1}{c\alpha_r} \quad (2)$$

where, τ_p and α_r are photon lifetime and loss per unit length, respectively. Thus, the loss per round trip is described as

$$\alpha = \alpha_r L = \frac{\omega}{cQ}L \quad (3)$$

We found the mode-locked condition with certain parameters. The mode-locked condition is equal to soliton formation in the time domain. Figure 3 clearly shows the evolution of soliton formation. In the time domain, pulses with sharp peaks are created and a 1-FSR frequency comb is formed in the frequency domain. On the other hand, we cannot see soliton formation in Fig. 4. This is because the input power is too high.
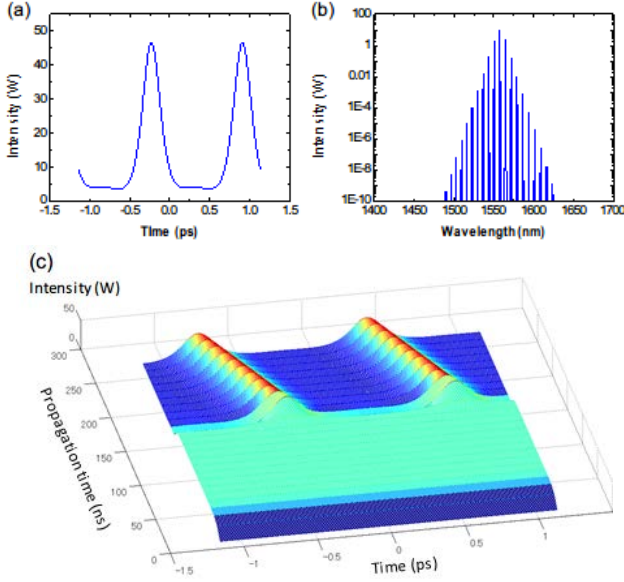
Fig. 3: Kerr comb simulation results. The main parameters are $Q_{\text{int}} = 2.0 \times 10^7, Q_{\text{couple}} = 2.0 \times 10^7, \delta_0 = 1.2 \times 10^{-4}, P_{\text{in}} = 1.5$ mW. (a) Temporal region (b) Spectral region (c) Pulse evolution in a microcavity.
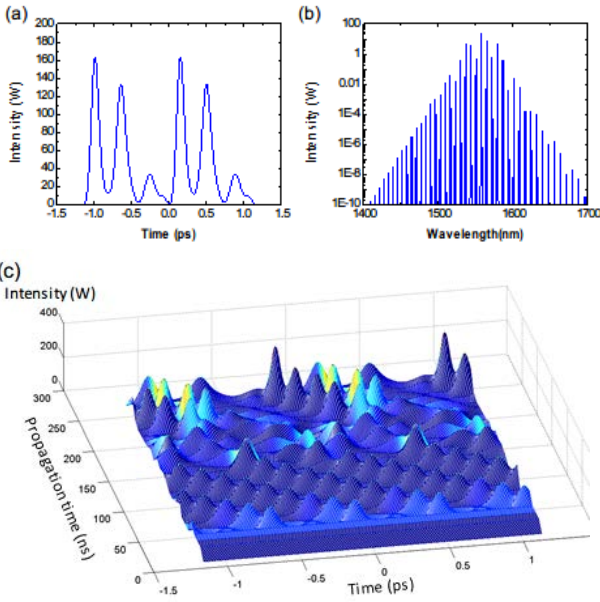

Fig. 4: Kerr comb simulation results. The main parameters are $Q_{\text{int}} = 2.0 \times 10^7, Q_{\text{couple}} = 2.0 \times 10^7, \delta_0 = 1.2 \times 10^{-4}, P_{\text{in}} = 30$ mW. (a) Temporal region (b) Spectral region (c) Pulse evolution in a microcavity.

2.3 Analytical results: bistability

A Kerr comb depends on many parameters including the individual characteristics of a cavity and the input power conditions. Given that these parameters affect the intracavity power of a microcavity, we should focus on optical bistability resulting from the optical Kerr effect. This is because optical bistability is particular feature of intracavity power.

Here, we analyze the relationship between bistable behavior and the Kerr comb conditions.

Optical bistability means that a microcavity can exhibit two states for the same input power. This behavior depends on the hysteresis of the input power. Figure 5 shows optical bistable behavior. The power of ① and ⑤ are different despite the input power being the same.
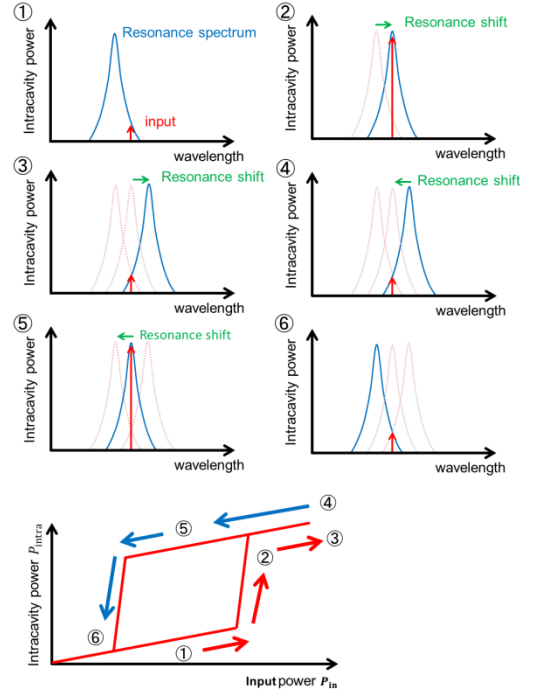

Fig. 5: Bistable behavior in a microcavity due to optical Kerr effect.

We gradually change the input power in order to include the bistability effect. Specifically, one input power is set until a steady state is achieved. The input power is then changed to the next value. We repeat this procedure. The time needed to achieve a steady state is $t_{\text{cal}} > 75\tau_{\text{p}}$. There are many patterns for the parameters needed for the simulation, and we introduce normalized detuning as $\Delta = \frac{2\delta_0}{\alpha + \kappa}$, which is normalized by the cavity losses.

Figure 6 shows the average intracavity power when the input power is gradually changed. When the input power is below 5.5 mW, four-wave mixing does not occur because of the low intracavity power. When the intracavity power increases rapidly as a result of the Kerr effect, 3-FSR harmonic mode locking is achieved. Furthermore, when the input power is increased above 8.5 mW, the mode locking is broken. When the input power is then reduced, 3-FSR mode locking is also achieved. We would like to emphasize that we can obtain 2-FSR mode-locked condition only when the input power is gradually decreased. We understand that hysteresis behavior is a key factor in controlling the Kerr comb condition. In particular, in this case we must reduce the decreasing to achieve a low FSR condition.
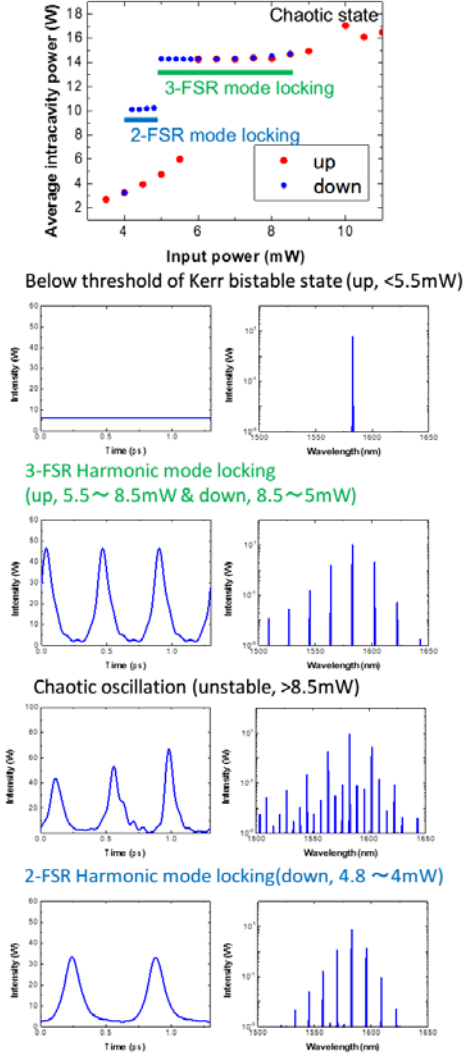
Fig. 6: The Kerr comb transition in a silica toroidal microcavity with $Q_{\text{int}} = 1.0 \times 10^7, Q_{\text{couple}} = 5.0 \times 10^7, \Delta = 2.2$. Red dots indicate the average intracavity power of the microcavity when the input power is increased from zero. Blue dots also indicate the average intracavity power when the input power is reduced from a high value.

3. Kerr comb generation experiment

By undertaking a simulation study, we found that the Kerr comb conditions can be controlled by controlling the parameters individual characteristic of a cavity and those of input. Here, we conducted Kerr comb generation experiments. Measuring a temporal waveform is an exact experiment for demonstrating Kerr comb generation. Before performing such an experiment, we measured the radio frequency (RF) signal of the Kerr comb. According to the report published by Herr et al., the RF signal indirectly shows whether or not the Kerr comb is mode-locked[7]. Figure 7 shows our experimental setup. We measured the optical frequency region of the Kerr comb with an optical spectrum analyzer and the radio frequency region is measured with an electrical spectrum analyzer.

The generation of RF noise has two causes. The one is Cavity-optomechanics (the cavity vibrates physically), the other is due to a developmental process of four-wave mixing. Figure 8 shows the measured optical and electrical spectrums. To compare with RF spectrums, above one has discrete RF spectrum, below one has continuous spectrum. We predict the above is caused by Cavity-optomechanics, the below is caused by both Cavity-optomechanics and a developmental process of four-wave mixing. In the future, we will research how Cavity-optomechanics influences the RF noise and aim to achieve the harmonic mode locking experimentally in good agreement with the numerical simulation results.
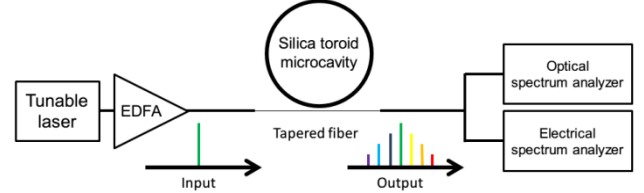
Fig. 7: Experimental setup for measuring radio frequency signal of optical Kerr comb.
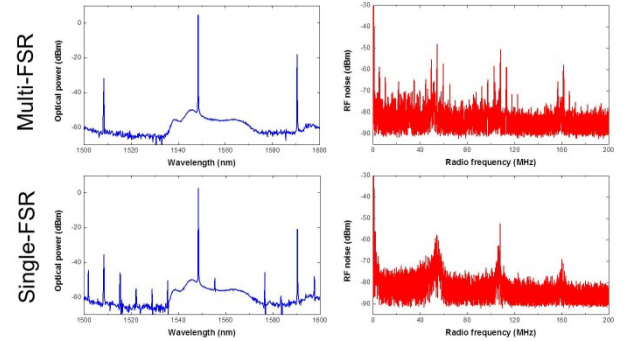
Fig. 8: Radio frequency measurement. We generate a comb with multi-FSR, then RF spectrum is discrete. On the other hand, a comb with single-FSR has continuous RF spectrum.

References

[1] P. Del'Haye, A. Schliesser, O. Arcizet, T. Wilken, R. Holzwarth and T. Kippenberg, Nature **450,** 1214 (2007).

[2] F. Ferdous, H. Miao, D. Leaird, K. Srinivasan, J. Wang, L. Chen, V. Aksyuk, and A. Weiner, Nat. Photon. **5,** 770 (2011).

[3] T. Herr, V. Brasch, J. Jost, C. Wang, N. Kondratiev, M. Gorodetsky, and T. Kippenebrg, Nat. Photon. **8,** 145 (2014).

[4] Y. Chembo, D. Strekalov, and N. Yu, Phys. Rev. Lett. **104,** 103902 (2010).

[5] S. Coen, H. Randle, T. Sylvestre, and M. Erkintalo, Opt. Lett. **38,** 37 (2013).

[6] L. Lugiato and R. Lefever, Phys. Rev. Lett. **58,** 2209 (1987).

[7] T. Herr, K. Hartinger, J. Riemensberger, C. Wang, E. Gavartin, R. Holzwarth, M. Gorodetsky, and T. Kippenberg, Nat. Photon. **6,** 480 (2012).

Stabilization of optical Kerr comb and construction of feedback system

Tomoya Kobatake (B4)   Ryo Suzuki (M1)

An optical frequency comb is usually generated with a solid laser or a fiber laser, and studies related to optical Kerr combs generated with a micro resonator are attracting interest. Here, we observed four wave mixing (FWM) generated in a silica toroid microcavity and constructed a feedback system with PID control to stabilize a Kerr comb formed by FWM.

Key words: Optical frequency comb; Nonlinear optics; Toroid cavity; Feedback control

1. Introduction

An optical frequency comb is a strictly equidistant and very broad spectrum which consists of equidistant lines similar to a comb in the frequency domain. In the time domain, it is a repeating femtosecond pulse train (Fig. 1). Optical frequency combs are called "rulers of light" because of their high accuracy and stability, and because they can be used as a scale that enables us to measure the frequency of light more easily. Moreover, we can expect them to be applied to spectroscopy, large capacity optical communication, optical clocks, and global positioning systems (GPS) [1]. Optical frequency combs are generated using a solid-state laser (Ti:sapphire laser) or a fiber laser and they provide highly accurate light sources. However, they are problematic in that they are large, expensive, and need a lot of energy. Therefore, we aim to realize small, low-cost, low energy, and highly accurate light sources using a Kerr comb or a pulse source with a high repetition rate. In this study, for Kerr comb application, we observed the generation of four wave mixing (FWM) and stabilized the optical coupling by PID control.
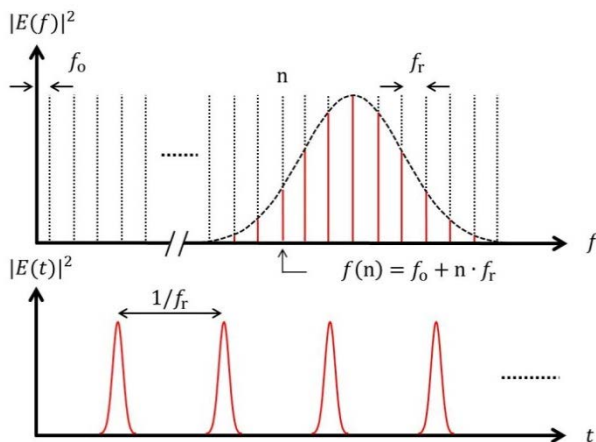

Fig. 1: Optical frequency comb in the frequency and time domains.

2. Principle of Kerr comb generation

The experimental setup for generating a Kerr comb is shown in Fig. 2. A single wavelength CW laser light is input into a microcavity, and the output is multiwavelength [2]. This spectral broadening is the result of FWM, which is a nonlinear optical effect that occurs in the cavity. FWM satisfies the energy conservation requirement.

$$\hbar\omega_1 + \hbar\omega_1 = \hbar\omega_2 + \hbar\omega_3 \qquad (1)$$
$$(\text{or } \hbar\omega_1 + \hbar\omega_2 = \hbar\omega_3 + \hbar\omega_4)$$

From equation (1) it is clear that ω_2 and ω_2 are symmetrical with respect to ω_1. When FWM is successively occurred, comb-like modes are constructed that are equidistant. However, we need to consider the dispersion of the resonator. If it has a flat dispersion, the resonant frequencies are equidistant thanks to the basic formula $nL = m\lambda$ (n: the refractive index, L: the cavity length, m = $1, 2, 3, \dots$), so they correspond to the frequency generated by FWM shown in Fig. 2 (b). On the other hand, if the dispersion is large, a Kerr comb is not generated because the frequency generated by FWM deviates from the resonant frequency shown in Fig. 2 (c).

Here we describe the conditions for generating FWM. FWM is a third-order nonlinear optical effect and it results when the electrical field density exceeds a certain threshold. This threshold of the input power into the cavity is given by

$$P_{threshold} \approx \frac{2\pi n^2 V}{\lambda n_2 Q^2} \qquad (2)$$

[3]. Q is the quality factor of the cavity, V is the mode volume, and n_2 is the nonlinear refractive index. So a high Q and a small mode volume enable the low power generation of FWM.

The above shows that, for the generation of FWM, ① a cavity can efficiently confine the light, ② the dispersion of the cavity is near the zero dispersion and ③ a high input power is required.
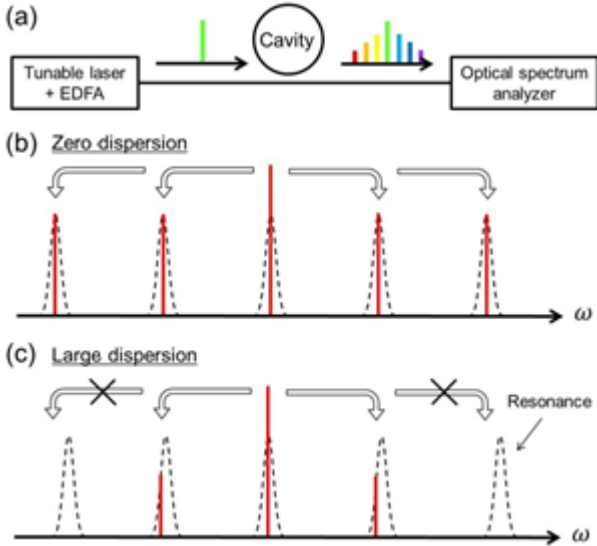
Fig. 2: (a) Experimental setup for Kerr comb generation. (b) (c) The spread of FWM in zero dispersion and large dispersion.

Fig. 3: Spectrum of generated Kerr comb.

3. Observation of Kerr comb generation

Here, we solve the problems listed in the preceding section. ① In this study, we used a silica toroid microcavity. We improved the fabrication and measurement process and the quality factor of the cavity became over $Q = 10^7$ from $Q = 10^6$. Theoretical analysis with equation (2) shows that an input power of over 1 W is needed with $Q = 10^6$, however, we can reduce the pump power threshold to 10 mW by using a cavity where $Q = 10^7$. ② We can determine the dispersion of the cavity as the sum of the material and structural dispersions. The former is defined by the material, in this case silica, and we coordinated the structure and controlled the dispersion at $\lambda = 1.55 \, \mu m$. ③ When a high power pump is input into the cavity, it generates heat and its refractive index (resonant wavelength) changes because of its expansion and the TO effect.

$$\Delta\lambda \approx \lambda(\alpha + \xi)\Delta T \qquad (3)$$

$\Delta\lambda$ is the shift of the resonant wavelength, ΔT is the variation in the cavity temperature, α is the expansion coefficient, and ξ is the thermo optic coefficient. Because of the resonance shift, pump laser cannot be inputted efficiently. So we swept the pump laser wavelength at 1 nm/s with the shift.] (If the laser is not input efficiently, FWM is not generated because the EDFA can output only 1 W). We improved the three points mentioned above and generated a Kerr comb whose spectrum is shown in Fig. 3. The cavity has $Q = 5 \times 10^6$, the input power is 200 mW, and the mode spacing is 850 GHz (= FSR of the cavity).
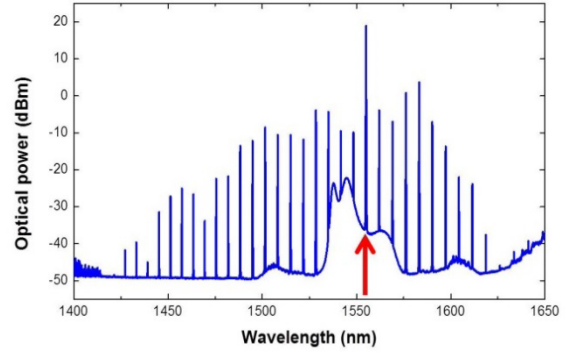We observed an FWM broadening of 200 nm.

4. Construction of feedback system

When we generated a Kerr comb, and we coupled the tapered fiber and cavity by closing them. However, the deformation of the equipment and the vibration of the tapered fiber causes the distance between them to change and the input power becomes unstable. If the input falls lower than the threshold, no Kerr comb is generated. A problem under actual conditions is that the Kerr comb disappears after a short time. To solve this problem, we constructed a feedback system to control the cavity position in relation to the comb power.

The temporal changes in the power when controlled at -27.5 dBm and without control are shown in Fig. 4. Without control, the power of the Kerr comb gradually decreased and had vanished after few minutes. On the other hand, the controlled Kerr comb power was fixed and continued for a longer time. Moreover, we moved the cavity about 100 nm in 340 s and 540 s in Fig. 4 to confirm the control, and we can see that the resulting power displacement is immediately fixed.

The program we created for the control system is based on PID control and it can be used for other control purposes?. For example if we use it to control the frequency, the power of the input laser or the temperature of the cavity, we will be able to stabilize the frequency of the Kerr comb.
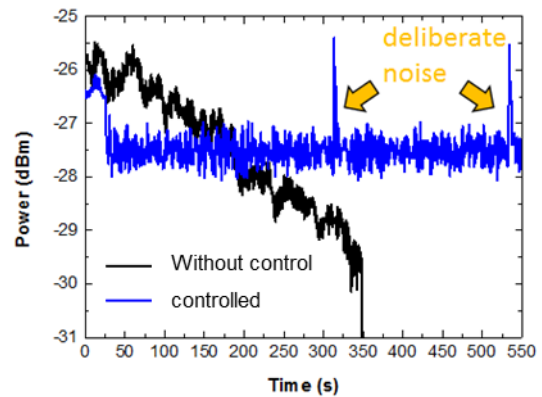

Fig. 4: Temporal change in power without control (black) and controlled (blue).

5. Conclusion

 We satisfied the condition for FWM generation by fabricating a silica toroid microcavity with a Q value of over 10^7 and generated a Kerr comb with a mode spacing of 850 GHz and a 200 nm spectrum. Moreover, we introduced a feedback system that enabled us to stabilize optical coupling and Kerr comb generation. This system can be used for many other purposes, and it will both support further study and lead to the creation of new applications.

References

[1] T. Udem, R. Holzwarth, and T. W. Hänsch, "Optical frequency metrology," Nature **416**, 233-237 (2002).

[2] P. Del'Haye, A. Schliesser, O. Arcizet, T. Wilken, R. Holzwarth, and T. J. Kippenberg, "Optical frequency comb generation from a monolithic microresonator," Nature **450**, 1214-1217 (2007).

[3] T. J. Kippenberg, S. M. Spillane, and K. J. Vahala "Kerr-nonlinearity optical parametric oscillation in an ultrahigh-Q toroid microcavity," Physical Review Letters **93**, 083904 (2004).

Demonstration of optical switching using the Kerr effect in a silica toroid microcavity

Wataru Yoshiki (M2)

We describe experimental results for all-optical on-chip switching using the Kerr effect in a silica toroid microcavity. Thanks to the high quality factor of the silica toroid microcavity, we achieved optical Kerr switching with an input power of 830 µW. Moreover, we show that this value can be reduced to 36 µW by employing a mode with a Q factor of $> 2 \times 10^7$. This switching power is the smallest among all previously reported on-chip optical Kerr switches.

Key words: Silica toroid microcavity; Kerr effect; Optical switch; nonlinear optics;

1. Introduction

All-optical switches based on an optical microcavity have been intensively studied with a view to replacing OEO conversion in current optical networks. Most optical switches employ the carrier-induced effect to modulate their refractive index. However, the response time of carrier-induced switching is limited by the finite carrier relaxation time. Moreover, they suffer from absorption loss originating from free carrier absorption (FCA).

Recently, several on-chip optical switches using the Kerr effect based on photonic crystal (PhC) [1] and microring [2] cavities have been reported. These switches are driven without generating any carriers. However, an input pump power exceeding 100 mW is required for switching in these devices because of their low quality factor ($<10^5$). To overcome this problem, some optical Kerr switches were developed by using whispering gallery mode (WGM) microcavities [3,4], which typically have a Q of $>10^8$. They require an input power of as little as 50 µW, but they appear to be difficult to fabricate on a chip.

In this work, we employed a silica toroid microcavity [5] that was fabricated on a chip and had a Q of higher than 10^6, and achieved an optical switching operation using the Kerr effect with an input pump power of 830 µW. Moreover, we show that a switching power of 36 µW is possible by using a mode with a Q of $> 2\times10^7$. This power is the smallest of all previously reported optical Kerr switches.

2. Experimental setup

Our silica toroid microcavity was fabricated using photolithography, SiO_2 etching, XeF_2 dry etching and laser reflow. First, a Si substrate with a 2 µm-thick layer of silica was prepared. Next, by using photolithography and SiO_2 etching, circular silica pads were formed on a Si substrate. Then, by employing XeF_2 dry etching, silica pads were under-cut and a silica disk on a silicon pillar was obtained. Finally, we employed a laser reflow process, and then fabricated a silica toroid microcavity. We fabricated a microcavity with major and minor diameters of about 70 µm and 4.5 µm, respectively. To couple the light into the microcavity, we employed the tapered fiber coupling method. The tapered fiber was fabricated by heating and stretching a commercially available single mode fiber. The fabricated tapered fiber typically had a diameter of 1 µm and a transmittance of 90%. We controlled the gap between the microcavity and the tapered fiber by using an automatic xyz stage with a resolution of 10 nm. This allowed us to precisely adjust the coupling between the microcavity and the tapered fiber.
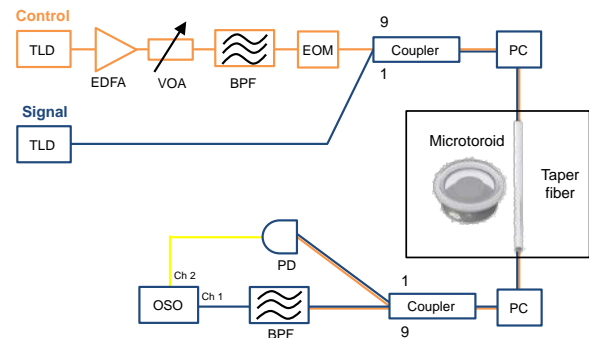
Fig. 1 Experimental setup for optical switching experiments.

Figure 1 shows a block diagram of our experimental setup. We used two lights; one as a control light and the other as a signal light. They were generated by different tunable laser diodes (TLDs), and their wavelengths were tuned to those of the different WGMs around 1550 nm in the silica toroid microcavity. We amplified the control light with an erbium doped fiber amplifier (EDFA). After that we modulated it into rectangular pulses with an electro-optical modulator (EOM). The control and signal lights were mixed at the coupler and inputted into the tapered fiber coupled to the

microcavity. The control light switches the signal light via the refractive index change in the microcavity. At the output, we filtered the control light out by using band pass filter (BPF), and then, detected only the signal output at an optical sampling oscilloscope (OSO). It should be noted that we also monitored the control output using a photo detector (PD) and the OSO to confirm that the control light was efficiently coupled into the microcavity. In addition, we placed polarization controllers (PCs) at the input and output of the tapered fiber to precisely match the polarizations of the input light and the desired WGM.

3. Optical Kerr switching operation

In a silica toroid microcavity, carrier generation is greatly suppressed thanks to the large bandgap or the silica (corresponding to $\lambda = 140$ nm). In addition, silica has negligible absorption loss (the corresponding Q factor related to the absorption Q_{abs} is 2×10^{11}). These characteristics enable us to use the Kerr effect in a silica toroid microcavity without considering other competing effects such as the carrier-induced effect and the thermo-optic (TO) effect. However, it is well known that the actual absorption of a silica-based microcavity is much larger than the material absorption [6]; this allows the TO effect to dominate the Kerr effect during a switching operation. Hence, it is necessary to distinguish between the TO and Kerr effects experimentally to achieve optical Kerr switching. To use the Kerr effect selectively, we take advantage of the large differences in the response times of the Kerr and TO effects. The response time of the Kerr effect is around a few tens of ns (limited by the cavity photon lifetime), but that of the TO effect is much longer than a μs in a silica toroid microcavity [7]. So we can use only the Kerr effect for the switching when we input control pulses whose duration is much shorter than the response time of the TO effect. When T_{cont} is too short for the TO effect to respond, only the Kerr effect contributes to the switching. In this situation the signal output exhibits fast switching behavior. On the other hand, when T_{cont} is long enough for the TO effect to respond, both the Kerr and TO effects are responsible for the switching. As a result, there are two switching slopes at the signal output; the faster one is caused by the Kerr effect and the other is caused by the TO effect. Thus, we can judge whether or not the switching is based on the Kerr effect by carefully analyzing the switching slope.

Figure 2(a) and (b) show the all-optical switching results for control pulse durations T_{cont} of 128 ns and 512 ns, respectively. Note that the loaded Q factors of the control and signal modes (Q_{cont}, Q_{sig}) are 3.3×10^6 and 5.1×10^6, respectively, and the input control peak power P_{in}^{cont} is 3.3 mW.

Figure 2(a) clearly shows that the signal output is switched to ON only when the control light is inputted. In addition, the signal output is switched to OFF after the control light is turned OFF. This ensures that we successfully achieved all-optical switching operation in a silica toroid microcavity. As seen in Fig. 2(a), the fall time of the signal output is 30 ns, which is much shorter than the thermal response time of > μs, and there is only a fast switching slope. Hence, this switching is due to the Kerr effect. On the other hand, there are two switching slopes, and the fall time is around 1 μs when the control pulse duration is 512 ns (Fig. 2(b)). In this situation, the Kerr and TO effects are responsible for faster and slower switching slopes, respectively. Hence, this switching is caused by a hybrid effect (Kerr and TO effects). From Fig. 2(a) and (b), we found that Kerr switching is possible in a silica toroid microcavity by employing control pulses that are much shorter than the thermal response time.
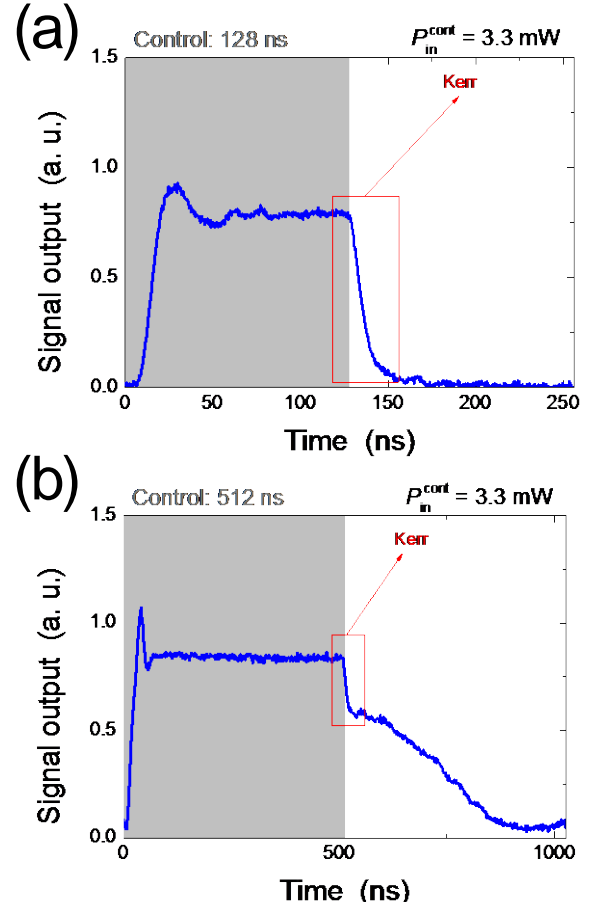
Fig. 2 Results of all-optical switching for control pulse durations T_{cont} of (a) 128 ns and (b) 512 ns. The blue solid line represents the signal output and the gray area indicates that the control pulse is inputted.

4. Required switching power

Here we show the input control power required for switching. Figure 3 shows the switching contrast for different input control powers when T_{cont} is 64 ns. Switching contrast is defined as the degree

to which the signal output is modulated in comparison with the reference level ("1" corresponds to complete modulation). The blue dots and black curve represent the experimental data and the theoretical curve. The theoretical curve is drawn by using the equations described in Ref. [7]. As seen in the graph, the theoretical curve agrees well with the experimental result. The theoretical curve considers only the Kerr effect (i.e. it neglects the TO effect), thus we quantitatively confirm that switching is based on the Kerr effect.

Figure 3 also shows that a switching contrast of 84% is achieved when the controlled input power P_{in}^{cont} is 5.3 mW (lower inset). On the other hand, switching is still observed when P_{in}^{cont} is reduced to 830 μW (upper inset). This is much lower than other on-chip optical Kerr switches based on a photonic crystal cavity [1] and a microring [2] that require input control powers of 200 mW and 1.1 W, respectively. Thus, our switch is the first on-chip Kerr switch that can be driven with an input control power of less than 1 mW.
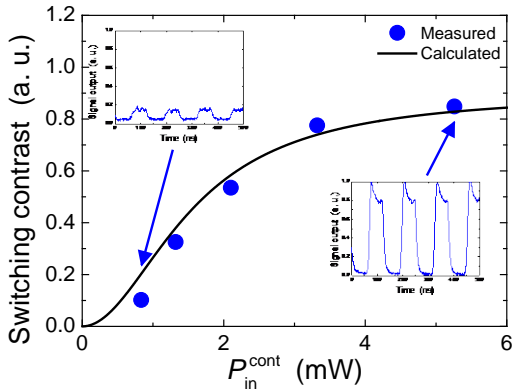

Fig. 3 Relationship between switching contrast and input control power. The blue dots and black curve represent the experimental data and theoretical curve, respectively. The upper and lower insets are the signal outputs for P_{in}^{cont} of 830 μW and 5.3 mW, respectively.
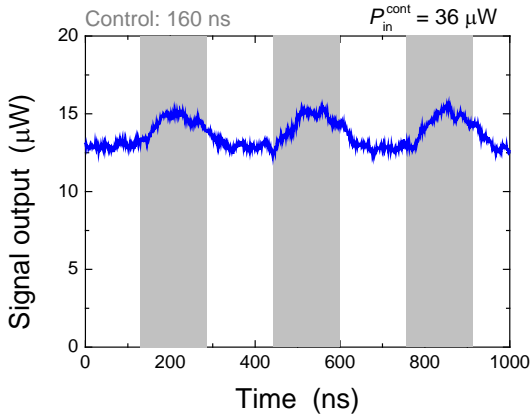

Fig. 4 Switching operation using WGMs with ultra-high Q factor.

It is worth noting that this low switching power is attributed to the high Q factor ($Q > 10^6$)

used in our experiments. So the switching power should be further reduced when we use a higher Q factor. With this in mind, we performed switching experiments using the WGM with $Q > 10^7$. Figure 4 shows the result of a switching experiment when we used WGMs with $Q_{cont} = 4 \times 10^7$ and $Q_{sig} = 2 \times 10^7$. The graph clearly shows that an optical switching operation is achieved for an input control power of 36 μW. This value is lower than that of optical Kerr switches with a high Q silica bottle microcavity, which requires a switching power of 50 μW [3]. To the best of our knowledge, the switching power of 36 μW is the lowest for any optical Kerr switch.

4. Conclusion

In summary, we demonstrated optical switching operation in a silica toroid microcavity using the Kerr effect. We found that optical Kerr switching is possible by inputting a control pulse whose duration is much shorter than the TO effect. In addition, we achieved optical switching with an input power of 830 μW. This value was reduced to 36 μW by employing WGMs with an ultra-high Q factor. This value is the lowest among all previously reported optical Kerr switches.

References

[1] V. Eckhouse, I. Cestier, G. Eisenstein, S. Combrié, G. Lehoucq, and A. D. Rossi, "Kerr-induced all-optical switching in a GaInP photonic crystal Fabry-Perot resonator," Opt. Express **20**, 8524–8534 (2012).
[2] J. S. Pelc, K. Rivoire, S. Vo, C. Santori, D. A. Fattal, and R. G. Beausoleil, "Picosecond all-optical switching in hydrogenated amorphous silicon microring resonators," Opt. Express **22**, 3797–3810 (2014).
[3] M. Pöllinger and A. Rauschenbeutel, "All-optical signal processing at ultra-low powers in bottle microresonators using the Kerr effect," Opt. Express **18**, 17764–17775 (2010).
[4] I. Razdolskiy, S. Berneschi, G. N. Conti, S. Pelli, T. V. Murzina, G. C. Righini, and S. Soria, "Hybrid microspheres for nonlinear Kerr switching devices," Opt. Express **19**, 9523–9528 (2011).
[5] D. Armani, T. Kippenberg, S. Spillane, and K. Vahala, "Ultra-high-Q toroid microcavity on a chip," Nature **421**, 925–928 (2003).
[6] M. Gorodetsky, A. Savchenkov, and V. Ilchenko, "Ultimate Q of optical microsphere resonators," Opt. Lett. **21**, 453–455 (1996).
[7] W. Yoshiki and T. Tanabe, "Analysis of bistable memory in silica toroid microcavity," J. Opt. Soc. Am. B **29**, 3335–3343 (2012).

Study of development of add-drop system and optical routing switch using silica toroid microcavity

Yui Yakushiji (B4)   Wataru Yoshiki (M2)

We developed an add-drop system using a silica toroid microcavity. Two optical taper fibers that are held separately by stage systems enabled us to arbitrarily control the coupling between the cavity and bus/drop optical taper fibers. In addition, we were able to switch optical routes using the developed add-drop system.

Key words: Silica toroid microcavity; Add-drop system; optical routing switch;

1. Introduction

An optical microcavity is a device that can strongly confine light and store it for long periods. The confinement strength and storage time are represented by the Q factor. Thus, a whispering gallery mode (WGM) cavity that has an ultra-high Q factor has attracted considerable attention. Recently, various WGM cavities with different geometries (e.g. spherical, bottle-shaped) and made of different materials (e.g. silica, crystalline, silicon) have been developed [1]. Among them, the silica toroid microcavity, originally developed by Armani *et al.* [2], attracted great interest because it can be fabricated on a silicon chip; this characteristic is beneficial in terms of integrating ultra-high Q cavities on a chip.

Of the many potential applications of a silica toroid microcavity, we focus on an add-drop filter. The ultra-high Q of the silica toroid cavity gives it the potential to be used as an ultra-narrow band filter. In addition, it is well known that this cavity can be coupled to a tapered optical fiber with negligible loss [3], and so this cavity can be used as an ultra-low loss filter. Rokhsari *et al.* [4] and Monifi *et al.* [5] have already reported the development of an add-drop filter using a silica toroid microcavity. However, in their studies the tapered fiber touched the cavity making it difficult to control the coupling (i.e. distance) between the cavity and the tapered fibers. There is a fundamental trade-off between transmittance and bandwidth (i.e. Q^{-1}) via the coupling in an add-drop filter. Hence, it is necessary to control the coupling to obtain the desired transmittance and bandwidth.

In this study, we developed an add-drop system using a silica toroid microcavity. The key to our study was to control the positions of two tapered fibers separately by using two independent stage systems. In addition, we were able to switch optical routes using the developed add-drop system. It is worth noting that no previous study has reported active operation in an add-drop system based on a silica toroid microcavity.

2. Development of add-drop system

When developing an add-drop system, we have to position two optical fibers with a gap between them of about the diameter of a silica toroid microcavity. However, this situation is difficult to achieve because the fiber holders of the two optical taper fibers interfere in such a situation. We avoid this interference by using a bent tapered optical fiber as a tapered drop fiber. Figure 1(a) shows a photograph of a bent tapered fiber. A bent tapered fiber is obtained by manually bending a fabricated straight tapered fiber. After it has been bent, it is attached to two slide glasses with double sided tape and UV adhesive. The bent tapered fiber becomes slack after the attachment, and this may cause vibration during optical measurement. Thus, we eliminate this slackness by increasing the gap between the two slide glasses d (Fig. 1(a)). It should be noted that we fix d at 20 mm because too large d introduces propagation loss as shown in Fig. 1(b).
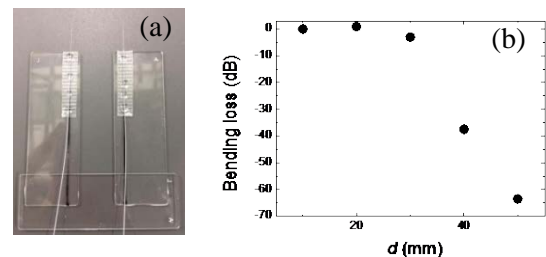

Fig. 1(a) Photograph of fabricated bent optical taper fiber and (b) measured propagation losses for different d values.

A fabricated bent optical fiber is attached to the newly developed stage system. This stage system includes an automatic piezo-driven *xyz* stage, thus allowing us to control the position of the bent tapered optical fiber with a resolution of a few tens of nanometers. In addition, the stage system also includes manual gonio- and rotation stages for adjusting the inclination in the horizontal and vertical planes. We can expect to obtain an arbitrary coupling condition by separately controlling the positions of tapered bus

and drop fibers.

3. Performance of add-drop filter

In this section, we evaluate the performance of the developed add-drop system. Figure 2 shows the experimental setup. The light output from the tunable laser diode (TLD) is input into port 1 of the bus optical fiber once its polarization has been adjusted with a polarization controller (PC). The outputs from port 2 of the bus fiber and port 3 of the drop fiber are then detected with a power meter (PWM).
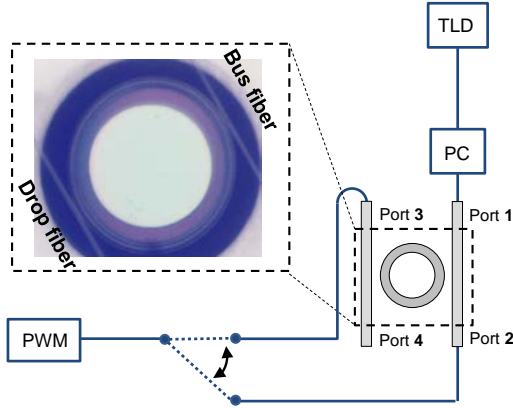

Fig. 2: Experimental setup. The inset shows a silica toroid microcavity with tapered bus and drop optical fibers.

Figure 3 shows the transmission spectra of the bus (port 2) and drop (port 3) tapered optical fibers. As seen in this figure, the bus output (black solid line) and drop output (red solid line) take 0 and 1 on the resonance, respectively. This indicates that only light whose wavelength is equal to the resonant wavelength is extracted from the bus fiber to the drop fiber. This behavior is clear evidence that our setup works successfully as an add-drop filter.
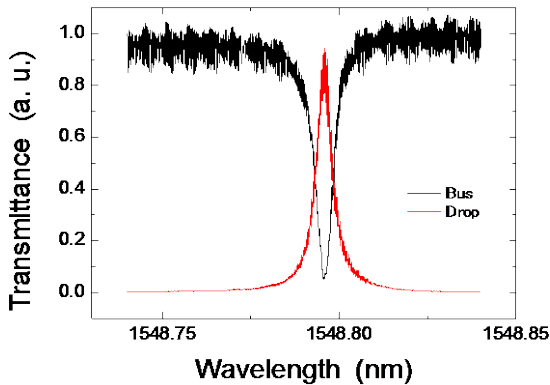

Fig. 3: Typical transmission spectra. The black and red solid lines represent the transmittance of the bus and drop fibers, respectively. Note that the curves are normalized by the off-resonance output from port 2.

Next, we confirm whether or not it is possible to control both transmittance and bandwidth (i.e. Q^{-1}) by adjusting the coupling between a cavity and tapered optical fibers. Figure 4 shows the transmittance of the drop fiber and the loaded Q factor for different gaps between the cavity and the drop fiber. In this figure, the transmittance increases while Q decreases when the coupling is stronger (i.e. the gap is smaller). On the other hand, the transmittance decreases and Q increases when the coupling is weaker (i.e. the gap is larger). Thus we confirmed experimentally that there is a trade-off between transmittance and Q factor. In addition to this, the figure clearly demonstrates that the transmittance and Q are controllable by carefully adjusting the coupling between the cavity and the tapered optical fibers. Moreover, as seen in Fig. 4, a maximum transmittance exceeding 90% is obtained when the gap is around 200 nm. This value is comparable to the value of 93% reported in Ref. [4].
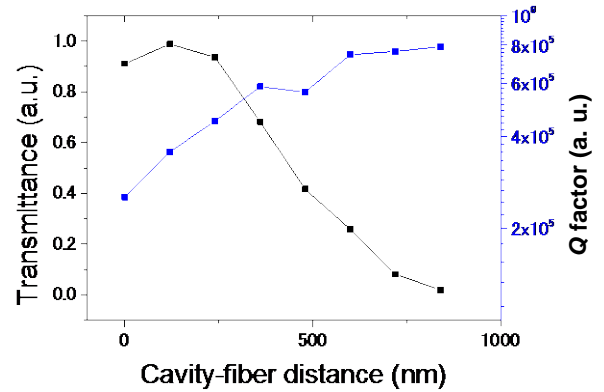

Fig. 4: The transmittance of the bus fiber (black solid line) and loaded Q factor (blue solid line) as a function of the gap between the cavity and the drop fiber. Note that the gap between the cavity and the bus fiber is fixed at 400 nm.

4. Optical route switching

Finally, we show the result of optical route switching, which is one of the applications of the add-drop system. Here, we briefly explain the principle of optical route switching. As shown in Fig. 3, most of the input power is output from the tapered drop optical fiber when the input wavelength is set at the resonant wavelength. However, the output from the bus fiber becomes large when the resonant wavelength shifts because here the input and resonant wavelengths are not matched. Thus, we can switch the output port (bus or drop) by somehow shifting the resonant wavelength. It is well known that the resonant wavelength of a cavity is proportional to its refractive index. With this in mind, in this study, we employed the Kerr effect, which changes the refractive index of the cavity, to achieve optical route switching.
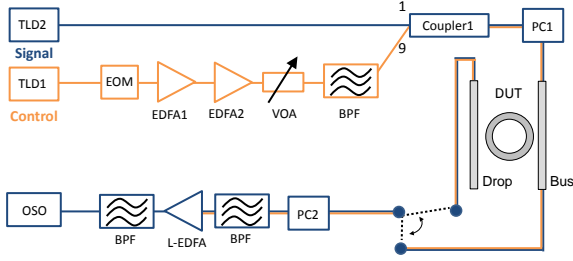
Fig. 5: Experimental setup for optical route switching.

Figure 5 shows the experimental setup. We have to input two lights to switch optical routes in a silica toroid microcavity; a weak "signal" light and a strong "control" light. The control light is used to induce the Kerr effect in the silica toroid microcavity and thus modulate the signal light output. A CW control light output from a TLD is amplified sufficiently by an Er-doped fiber amplifier (EDFA) to induce the Kerr effect after being modulated into rectangular pulses by an electro-optic modulator (EOM). The signal and control lights are then mixed and input into the silica toroid microcavity. The control lights output from the bus and drop fibers are removed with a band-pass filter (BPF), thus only the signal light is detected by an optical sampling oscilloscope (OSO) after being amplified by the L-band EDFA.

Figure 6 shows the signal light output from the bus and drop fibers. The control and signal lights are input into the WGMs with a Q of around 3×10^6. In addition, the input power of the control light P_{in}^{cont} is 63 mW and the pulse duration T_{cont} is 32 ns. As seen in Fig. 6, the output from the bus (black solid line) and drop (red solid line) fiber behave in opposite ways. In addition, the ON and OFF of both outputs are switched when the control light is input (indicated by gray area). These two behaviors indicate that we can achieve optical route switching using our developed add-drop system.

5. Conclusion

In this study, we developed an add-drop system using a silica toroid microcavity. We confirmed that the coupling in the system was controllable. Thanks to this feature, arbitrary transmittance and Q values can be obtained by adjusting the coupling. In addition, we reported the results of optical route switching as an application of the developed system. This is the first demonstration of active operation in an add-drop system using a silica toroid microcavity.

References

[1] K. Vahala, "Optical microcavities," Nature **424**, 839-846 (2003).
[2] D. Armani, T. Kippenberg, S. Spillane, and K. Vahala, "Ultra-high-Q toroid microcavity on a chip," Nature **421**, 925-928 (2003).
[3] S. Spillane, T. Kippenberg, O. Painter, and K. Vahala, "Ideality in a fiber-taper-coupled microresonator system for application to cavity quantum electrodynamics," Phys. Rev. Lett. **91**, 043902 (2003).
[4] H. Rokhsari and K. Vahala, "Ultralow loss, high Q, four port resonant couplers for quantum optics and photonics," *Phys. Rev. Lett.* **92**, 253905, (2004).
[5] F. Monifi, J. Friedlein, S. K. Ozdemir, and L. Yang, "A robust and tunable add-drop filter using whispering gallery mode microtoroid resonator," J. Light. Technol. **30**, 3306-3315 (2012).
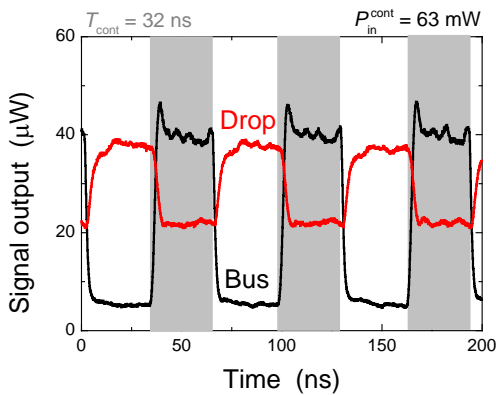
Fig. 6: The signal output from the bus (black solid line) and the drop (red solid line) fibers. The gray area indicates that the control light is input.

Examination of the transmission of a broadband pulse through an ultrahigh-Q nanocavity

Zhelun Chen（B4）　Fushimi Akihiro（M1）　Wataru Yoshiki（M2）

The resonance spectrum of a nanocavity is shifted toward the low frequency side by the Kerr effect when light is stored in the nanocavity. We succeeded in transmitting broad bandwidth pulses through an ultrahigh-Q nanocavity by making the instantaneous frequency of the input chirped pulse accord with the shifting resonance frequency. We also observed the effect of adiabatic wavelength conversion.

Key words: Nanocavities; Chirped pulses; Kerr effect; Adiabatic wavelength conversion;

1. Background

An all-optical switch with nanocavities has been actively studied [1], but there is a problem. That is, the Q factor of the nanocavities and the signal transaction speed are related to the transactions, because the resonance spectrum of a high-Q nanocavity is narrow although the spectrum of short light pulses is broad. Some research has been undertaken with a view to solving this problem by dynamically changing the Q factor [2-3], but the approach required active operation and a complicated structure.

Our aim was to transmit a short pulse, namely a pulse with a broadband spectrum, through an ultrahigh-Q nanocavity without active operation or a complicated structure.

2. Transmit broadband pulse by Kerr effect

Although it is impossible to store a pulse whose spectrum is broader than the resonance frequency in a nanocavity, we used the Kerr effect to transmit such a pulse.

$$n = n_0 + n_2 I \tag{1}$$

The Kerr effect is a phenomenon whereby the refractive index n increases in proportion to the electric field strength density I and the nonlinear optical effect coefficient n_2.

The resonance spectrum shifts to the low frequency side as a result of the Kerr effect. So it is possible to store a broadband pulse that is broader
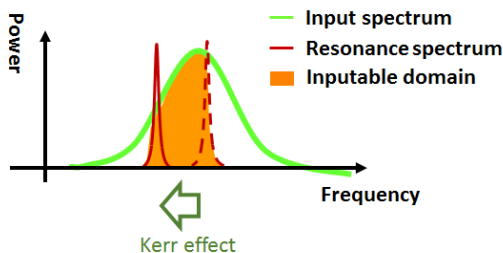
than the resonance spectrum in an ultrahigh-Q nanocavity, if the instantaneous input frequency matches the shifting resonance frequency as shown in Fig. 1.

2. Effective storage with chirped pulse

When inputting Fourier limit pulses, whose frequency is constant, we cannot effectively store a pulse in a nanocavity, because the resonance frequency shifts as a result of the Kerr effect. Therefore, we focused on the spectrum phase. We aimed ideally at setting the spectrum phase of the input chirped pulse, whose instantaneous frequency is the same as the shifting resonance frequency.
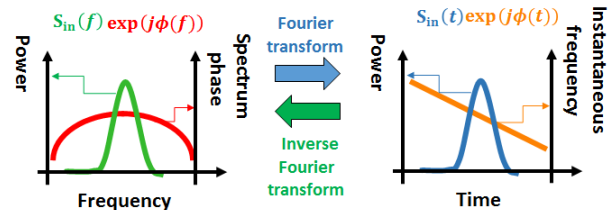

Fig. 2: With a Gauss type spectrum and a quadratic function spectrum phase, the temporal waveform of this spectrum is also Gauss type and its instantaneous frequency changes linearly according to the Fourier transform relations.

3. Analysis of add-drop system with coupled mode theory equation

We numerically analyzed an add-drop system with the coupled mode theory (CMT) equation (eq. 2) to verify the method of storing the broadband pulse using the abovementioned principle.

We took S_{in} shown in Fig. 3 as a chirped pulse, and numerically analyzed the output of the drop side S_{out2} with the CMT equation (eq. 2).

$$\frac{da(t)}{dt} = \left(\frac{j2\pi c}{\lambda_{\text{cavity}}} - \frac{1}{2\tau} \right) a(t) + \sqrt{\frac{1}{\tau_{\text{coup1}}}} e^{j\theta} s_{in}(t) \tag{2}$$

Fig. 1: Rough sketch of the transmission of the broadband pulse induced by the Kerr effect.

$a(t)$ shown in (eq. 2) is the electric field in the nanocavity and $\lambda_{\text{cavity}}(t)$ is the resonance wavelength considered Kerr effect. τ is the photon life of the nanocavity and τ is expressed as $\tau_{\text{coup1}}^{-1} + \tau_{\text{coup2}}^{-1} + \tau_{loss}^{-1}$. $s_{\text{in}}(t)$ is the input electric field and θ is the phase difference between $a(t)$ and $s_{\text{in}}(t)$.
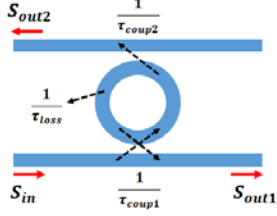

Fig. 3: Schematic chart of add-drop system. S_{in} is the input pulse, S_{out1} is the transmitted pulse and S_{out2} is the output of the drop side. . τ_{coup1} and τ_{coup2} are the photon lifetimes corresponding to the combination with waveguides and τ_{loss} is the photon lifetime corresponding to the loss caused by leakage from the waveguides or the absorption of the material.

4. Design suitable pulse by spectrum domain modulation

We considered a pulse with a Gauss type spectrum. The input pulse needs a suitable spectrum phase to be stored effectively in nanocavities as stated above. We assumed pulses with a quadratic function spectrum phase. We fixed the absolute value of the spectrum as Gauss type but changed the spectrum phase and the detuning between the central frequency of the input pulse and the resonance frequency, and then we numerically analyzed S_{out2} (Fig. 4).

We also analyzed the instantaneous input frequency and the S_{out2} and S_{in} spectra, which have a suitable spectrum phase. We show these graphs below.

The instantaneous input frequency changes linearly as in Fig. 5(a) because its spectrum phase is a quadratic function. As shown in Fig. 5(b), the spectrum of S_{out2} of the chirped pulse (red line) is broader than the spectrum of S_{out2} of Fourier limit pulses without the Kerr effect (orange line), the spectrum of S_{out2} of Fourier limit pulses with the Kerr effect (blue line) and the resonance spectrum (black line).

When we input the most suitable chirped pulse (Fig. 4(b) red dotted line), the output is S_{out2} (Fig. 4(b) red solid line), and the FWHM of the temporal
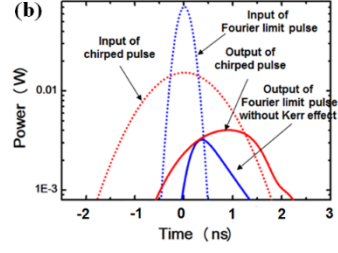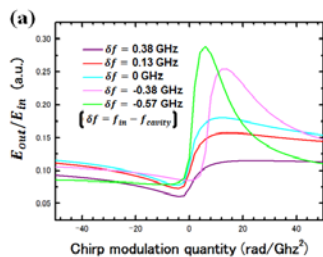

Fig. 4: (a) The energy ratio of S_{out2} and S_{in}, which has the same absolute spectral value and a different spectrum phase and detuning (δf). The input energy is 28.4 pJ and the FWHM of the input is 1.2 GHz. The assumed resonance frequency of the cavity is 194 THz, the Q factor is 7.5×10^5 and $\tau_{coup1} = 1.23$ ns, $\tau_{coup2} = \tau_{loss} = 2.46$ ns. When δf is -0.57 GHz and the spectrum phase is 4.5 rad/ GHz^2, the energy of S_{out2} is the largest. (It is 28.4 % of the energy of S_{in}.) (b) The temporal waveforms of S_{out2} and when inputting the chirped pulse with the spectrum phase 4.5 rad/ GHz^2 and δf =-0.57 GHz,, and when inputting a Fourier limit pulse with δf =-0.57 GHz..
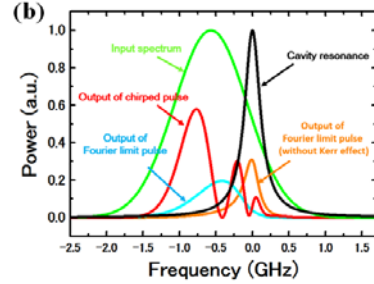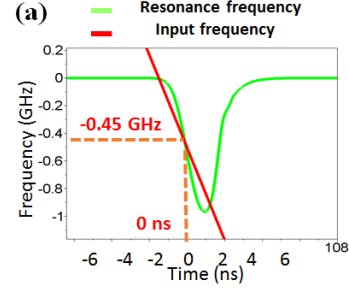

Fig. 5: (a) The resonance frequency and the input frequency when δf is -0.57 GHz and the spectrum phase of input is 4.5 rad/ GHz^2, where the S_{out2} energy is the largest. When it is 0 ns, the resonance frequency shift -0.45 GHz and the resonance frequency and the input frequency agree. (b)The spectra when δf is -0.57 GHz and the spectrum phase of input is 4.5 rad/GHz^2. In addition, it is assumed that the center of the resonance spectrum is 0 GHz.

waveform becomes about 500 ps.

Based on the above, we succeeded in designing a suitable chirped pulse with a spectrum, whose absolute value is Gauss type.

5. Adiabatic wavelength conversion

The transmissivity of the add-drop system, which we set in a steady state in this study, is approximately 50%, but with the S_{out2} spectrum of

the chirped pulse (Fig. 5 (b) red line), the transmissivity of the spectrum is 62 % at -0.75 GHz. We considered this to result from the effect of adiabatic wavelength conversion.

When light is stored in a nanocavity, if the resonance frequency is shifted by nonlinear optical effects before the light leaks from the nanocavity, the frequency of the light also shifts. This is adiabatic wavelength conversion.

Figure 5(a) shows that the input frequency and resonance frequency are the same at -0.45 GHz, and the resonance frequency shifts the more rapidly. In addition, Fig. 5(b) shows that the power of the S_{out2} spectrum of the chirped pulse (red line) is 0 W. From the above, we considered that adiabatic wavelength conversion was caused by the Kerr effect just after the chirped pulse was stored in the nanocavity when the instantaneous frequency was -0.45 GHz. Therefore, the frequency of the light stored in the nanocavity shifted toward the low frequency side before it leaked out. As a result, the power of the spectrum at -0.45 GHz is 0 W. We considered that the power of the shifted light was added to the power of the spectrum at -0.75 GHz, so the transmissivity of the spectrum is 62 % at -0.75 GHz.

6. Design suitable pulse by temporal domain modulation

We also considered a case where the temporal waveform is Gauss type.

We focused on the instantaneous frequency (instantaneous wavelength) of the input pulse. In accordance with the above principle, if the
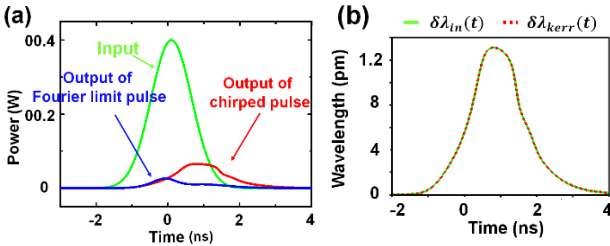

Fig. 6: (a) The input $S_{in}(t)$ (green line), S_{out2} when $s_{in}(t)$ is a Fourier limit pulse (blue line) and S_{out2} when $s_{in}(t)$ is the most suitable chirped pulse derived by the algorithm in Fig. 8. (b) The instantaneous wavelength shift of the input and the resonance wavelength shift. These are equal.

instantaneous wavelength of the input pulse and the resonance wavelength are the same, broadband pulses can be transmitted through high-Q nanocavities. We set the temporal waveform of the pulse as Gauss type, and then derived the most suitable instantaneous wavelength using the algorithm shown in Fig. 8. (The numerical value is the same as in Fig. 4).

By using the algorithm shown in Fig. 8, we made the instantaneous input wavelength and the
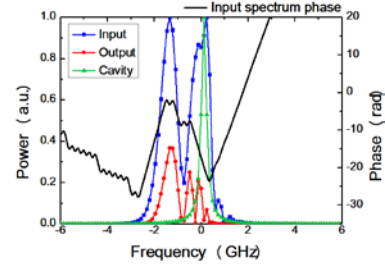

Fig. 7: The spectrum of $s_{in}(t)$ with the most suitable instantaneous wavelength derived by the algorithm in Fig. 8 (blue line), the spectrum of S_{out2} and the resonance spectrum ($S_{in}(t)$ is green line in Fig. 6(a)). The black line is the spectrum phase of $s_{in}(t)$.
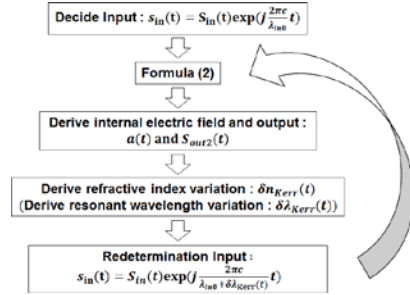

Fig. 8: Schematic chart of the algorithm for designing a suitable pulse by temporal domain modulation. This algorithm is intended for the add-drop system shown in Fig. 3. First, we set the amplitude $s_{in}(t)$ of the input pulse $s_{in}(t)$ and the central wavelength λ_{in0}, and then derived the electric field in the nanocavity $a(t)$ and the output $S_{out2}(t)$ with (eq. 2). We then derived the refractive index change $\delta n_{Kerr}(t)$ in the nanocavity and the resonance wavelength change $\delta\lambda_{Kerr}(t)$ from $a(t)$. Next, we reset $s_{in}(t)$, to make the instantaneous wavelength change of $s_{in}(t)$ agree with $\delta\lambda_{Kerr}(t)$. Finally, we reset $s_{in}(t)$ to (eq. 2). By repeating this operation, the instantaneous wavelength of input and the resonance wavelength become the same.

resonance wavelength equal. As a result, we succeeded in transmitting 21.5 % of the input energy through a high Q nanocavity. This value is three times greater than the output energy of the input pulse, which is a Fourier limit pulse with the same amplitude.

When we set the dispersion compensation for S_{out2} (Fig. 6(a) red line), the FWHM of the temporal waveform becomes about 300 ps.

Based on the above, we succeeded in designing a suitable chirped pulse with a Gaussian temporal waveform.

References

[1] K. Nozaki, et al., Nature Photon. **4,** 477 (2010).
[2] Q. Xu, et al., Nature Phys. **3,** 406 (2007).
[3] Y. Tanala, et al., Nature Materials. 6, 862 (2007)

Study of measurement in liquid environment using 780 nm laser for sensing application

Ryuusuke Saito (M1)　Jiro Nishimura (M1)

A silica microcavity has the potential to provide a highly sensitive chemical sensor or biosensor, and measurements in liquid environments are necessary for sensing applications. In this report, we describe measurements performed in a liquid environment.

Key words: Measurement in liquid environment; Sensing; Optical microcavity

1. Introduction

A silica microcavity can enhance the interaction between light and matter because of its high Q factor, thus making it a candidate for a highly sensitive sensor [1],[2]. In particular, measurements in liquid environments are needed for chemical sensing where chemical substances are detected or for biosensing where viruses and cells are detected. To this end, we devised and demonstrated a technique for undertaking measurements in liquid environments.

2. Study of optical tapered fiber

We calculated the optimal thickness of a tapered fiber in a liquid environment consisting of pure water [3].

The single mode condition of a cylindrical step-index optical fiber is represented as

$$V = k_0 n_1 a \sqrt{2\Delta} < 2.405 \tag{1}$$

Where V is the V-parameter. Here, n_1 is the refractive index of the cladding 1.44, and n_2 is the refractive index of pure water 1.33. Here, we could not use the weakly guiding approximation and instead used the following equation.

$$\Delta = \frac{n_1^2 - n_2^2}{2n_1^2} \tag{2}$$

Using
$k_0 = 2\pi/\lambda$, $n_1 = 1.44$, $n_2 = 1.33$, $\lambda = 780$ nm, we obtained

$$a < 0.54 \times 10^{-6} \text{ mm} \tag{3}$$

From this result, we obtained the single mode condition in a liquid environment as

$$2a < 1.08 \times 10^{-6} \text{ mm} \tag{4}$$

In this experiment, we fabricated a tapered fiber of the same thickness as (4).

3. Transmittance spectra measurement in liquid environment

A 1550 nm band laser was unsuitable for experiments in liquid environments due to its large absorption of water, and so we used a 780 nm band laser. Figure 1 shows the appearance of the experiment in a liquid environment, and Fig. 2 shows the transmittance spectrum of a silica toroid microcavity in air and pure water.
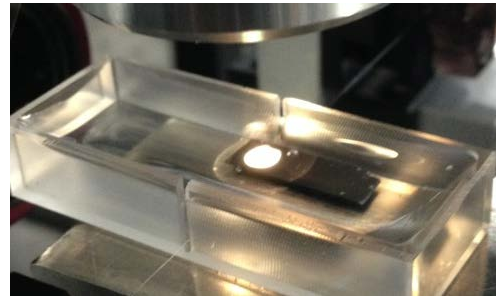
Fig. 1: Photograph of experiment in liquid environment.
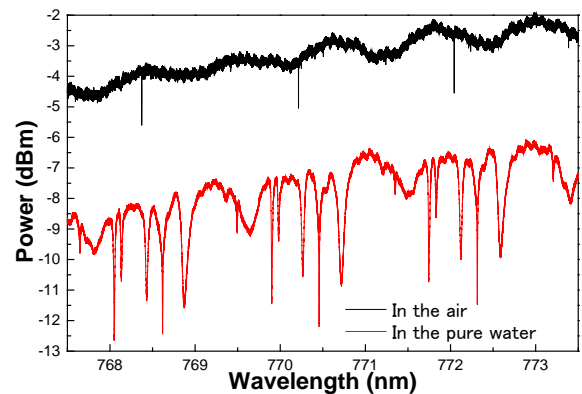
Fig. 2: Transmittance spectra of silica toroid microcavity. The black line shows the result in air and the red line shows the result in pure water.

As seen in Fig. 2, the transmittance rate of the tapered fiber decreased by 4~5 dB. Moreover, the Q factor fell from 10^6 to 10^4 and excited a lot of higher order modes. Drops in the transmittance rate of the tapered fiber and the Q factor were due to the absorption of pure water, and the excitement of higher order modes resulted from the small

refractive index contrast between the silica toroid microcavity and pure water.

4. Measurement of refractive index change

by medium

 One of the purposes of performing measurements in a liquid environment is to realize biosensing applications such as the detection or analysis of viruses or cells. With cell analysis, we have to undertake measurements in a medium.

 In this experiment, we added medium little by little and investigated the change in refractive index by measuring the resonant wavelength shift. Because a tapered fiber is affected by surface tension when it is moved from a liquid into the air, we kept the fiber in the liquid and measured the transmittance spectrum. Figures 3 and 4 show the transmittance spectrum in pure water and after the fiber was placed in the medium, respectively.
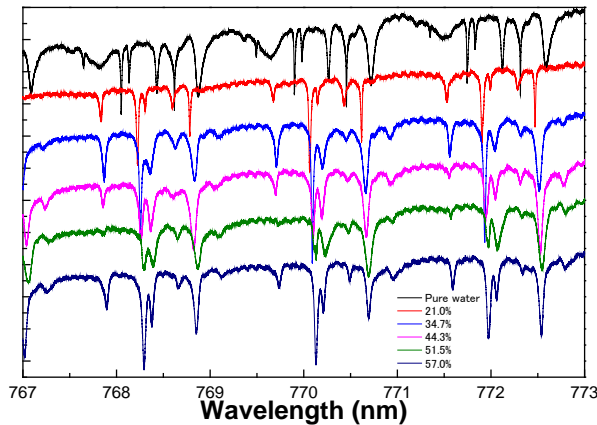
Fig. 3: Transmittance spectra of silica toroid microcavity. The black line is the spectrum in pure water and the lower spectra were obtained after increasing amounts of medium.
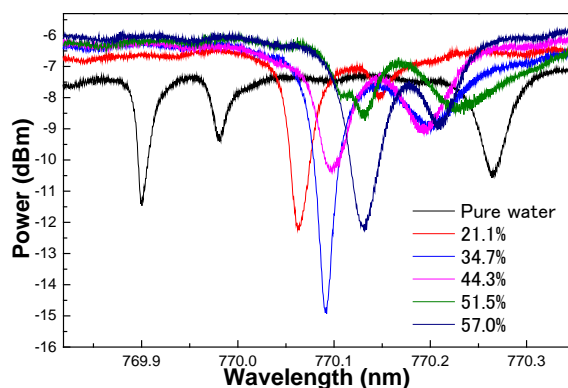
Fig. 4: Transmittance spectrum incorporating the results in Fig. 3.
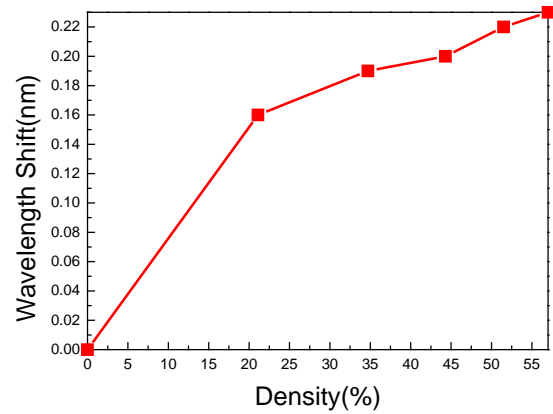
Fig. 5: Resonant wavelength shift depending on density of medium.

 Figure 4 shows that the resonant wavelength became longer as the density of the medium increased. This was because the medium has a higher refractive index than pure water. In terms of the Q factor, a value of 5×10^5 has been reported for a silica microcavity. In our experiment, the Q factor was one-tenth of this value and must be improved to realize higher sensitivity.

References

[1] F. Vollmer and S. Arnold, Nature Method **5**, 591 (2008).
[2] F. Vollmer, S. Arnold and D. Keng, Proceedings of the National Academy of Sciences **105**, 20701 (2008).
[3] Y. Kokubun, "Kouhakougaku," Kyouritusyuppan Co. (1999).

Shape manipulation and surface treatment process for crystalline WGM resonators to obtain higher *Q*

Yosuke Nakagawa (B4)   Hiroshi Kudo (M2)

When we fabricate WGM microcavities with the laser-heated pedestal growth (LHPG) method, the use of crystalline material results in polygonal cavities. Last year, we showed that the shape could be changed from a hexagon to a circle. Here, we describe theoretically how to fabricate a circular shape and realize quantitative fabrication by changing the angle of the seed rod. In addition, resonators fabricated by crystal growth have a rough surface and so we attempt to reduce this roughness by etching.

Key words: Crystal growth, Whispering gallery mode, shape manipulation, etching

1. Introduction

The laser heated pedestal growth (LHPG) method is a technique used with the Czochralski method (CZ method), and was developed to realize thinner, longer, and more uniform crystal fiber [1]. We form a bulge   by controlling the seed rod and feed rod velocity ratio. The bulge can excite light as a microcavity. As a result, we successfully fabricated a crystalline resonator using the LHPG method [2]. Last year, we analyzed the relationship between *Q* and the curvature radius of the microcavities, and found that it is easier for a circular shape to confine light efficiently in the WGM mode. However, the crystalline material makes the shape of the cavities polygonal. A cavity fabricated with sapphire is hexagonal. We fabricated the circular shape by heating the seed rod prior to crystal growth. But we could not understand theoretically why the circular shape was fabricated and we could not fabricate quantitatively. So we researched the theory behind this phenomenon.

2. Theory of circular shape fabrication

In crystal growth, the resonator shape must be made as stable as possible using the lowest possible energy. This shape obeys Wulff's theorem as shown in Eq. 1 by using the surface energy possessed by the crystal plane. Wulff's equation describes the relationship between surface energy and distance from the center of a crystal. As the surface energy decreases, the distance between the crystal plane and the center of the crystal decreases. The crystal plane is positioned as seen in Fig. 1 according to Wulff's theorem. This crystal plane forms a polygon as in Fig. 1 and this is called an equilibrium shape. An equilibrium shape has the lowest energy, so the cross-sectional shape is an equilibrium shape during crystal growth. There are many crystal planes in a crystal structure. Therefore, the equilibrium shape differs depending on the angle from which the crystal structure is viewed. Fig. 2 compares the equilibrium shape with the cross-sectional shape using sapphire crystal growth at the same angle. The equilibrium shape is associated with a cross-sectional shape in crystal growth.

$$\frac{\sigma_{001}}{h_{001}} = \frac{\sigma_{101}}{h_{101}} = \frac{\sigma_{100}}{h_{100}} = const \qquad (1)$$
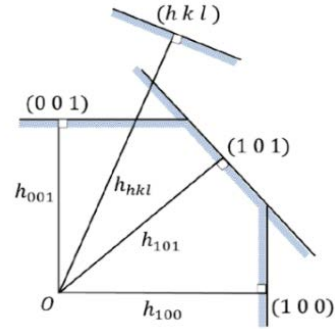
Fig. 1 Schematic illustration of the method for calculating an equilibrium shape from Wulff's theorem.
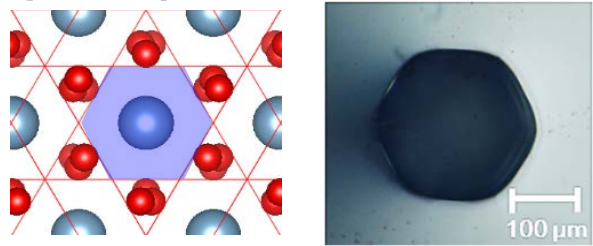
Fig. 2 Equilibrium shape and cross-sectional shape against c-axis.

The crystal structure of sapphire is shown in Fig. 3. Sapphire has 38 crystal planes as shown in Tab. 1. Tab. 1 shows X-ray analysis results obtained for sapphire [2]. α is the angle of the crystal plane against the a-axis as shown in Fig. 4. β is the angle of the crystal plane against the c-axis as also shown in Fig. 4.

Fig. 3 Crystal structure of sapphire.

Tab. 1 Crystal planes of sapphire.

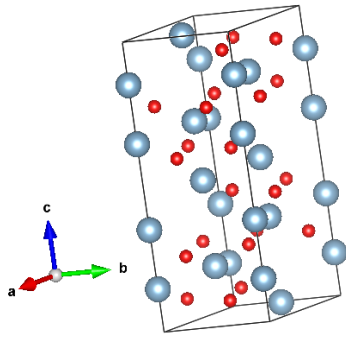| h	k	i	α	β	h	k	i	α	β
1	1	0	60	0	1	2	5	71	31
2	2	0	60	0	0	1	2	90	32
4	1	0	40.9	0	0	2	4	90	32
3	0	0	30	0	0	3	6	90	32
3	2	1	53.4	4.16	3	1	8	44	35
1	3	1	76.1	5.03	2	2	9	60	39
2	1	1	49.1	6.84	1	2	8	71	44
0	4	2	90	9.01	1	1	6	60	48
3	1	2	43.9	9.98	2	1	10	49	50
1	2	2	70.9	13.5	1	0	4	30	52
2	2	3	60	15.4	2	0	8	30	52
3	2	4	53.4	16.2	1	2	11	30	53
2	0	2	30	17.6	0	2	10	30	58
4	0	4	30	17.6	1	1	9	30	59
1	3	4	76.1	19.4	1	1	12	30	66
2	3	5	66.6	20	0	1	8	30	68
2	1	4	49.1	25.6	1	0	10	30	73
1	1	3	60	28.8	0	0	6	30	90
2	2	6	60	28.8	0	0	12	30	90
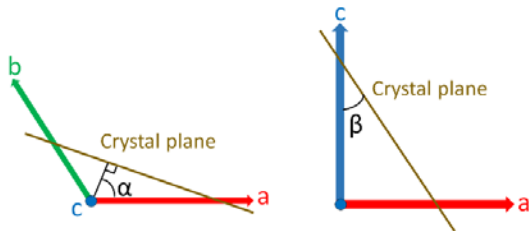
Fig. 4 Schematic illustration of crystal plane angle.

If the equilibrium shape is circular, the cross-section of the resonator is also circular. However, the equilibrium shape is constructed from crystal planes and is a polygon. This means the equilibrium shape, which is nearly circular, is a regular polygon with many corners.

The number of corners increases with the number of crystal planes that affect the equilibrium. If the angle to tilt a seed rod is near the angle of the c-axis of the crystal plane, this crystal plane affects the equilibrium shape. There are many crystal planes at 30 degrees as shown in Fig. 4.

And if the equilibrium shape is affected by the crystal planes, which have different angles as seen in the right image in Fig. 5, the equilibrium shape is almost circular.
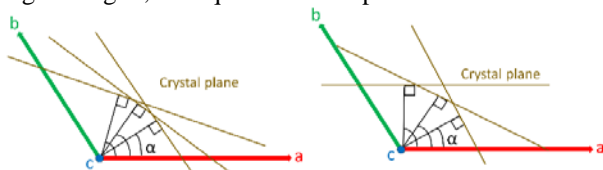

Fig. 2 Angle for a-axis of crystal plane

We calculated a suitable angle based on the above two conditions, namely that we had a regular polygon and many corners. The suitable angle is approximately 30 degrees.

3. Shape manipulation

The equilibrium shape differs depending on the angle at which you see the crystal structure, so we fabricated the resonator by changing the angle of the seed rod during crystal growth as shown in Fig. 6. And the resonators we fabricated in this way are shown in Fig. 7.
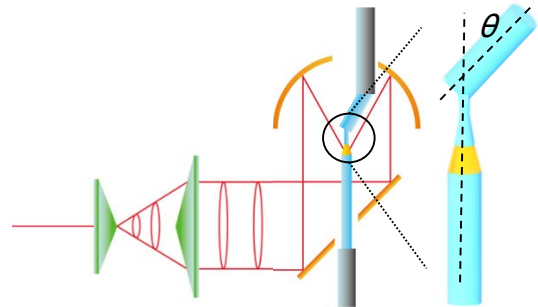
Fig. 6 Experimental setup changing the seed rod's angle.
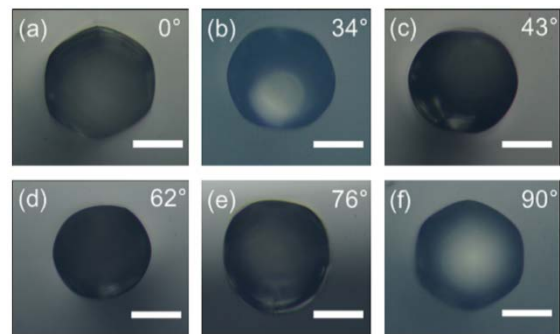
Fig. 7 Cross-sectional shape with respect to different crystal axes. The white line is 100 μm (a) θ of 0 ° (b) θ of 34 ° (c) θ of 43 ° (d) θ of 62 ° (e) θ of 76 ° (f) θ of 90 °

4. X-ray analysis

X-ray analysis showed that the resonator consisted of crystal planes in accordance with the theory. It was 50 % that we fabricated theoretically. By comparison with the theory, one of the resonator's crystal planes is shifted 40 degrees. The X-ray analysis results show that the cross-sectional shape is almost circular as in Fig. 6.
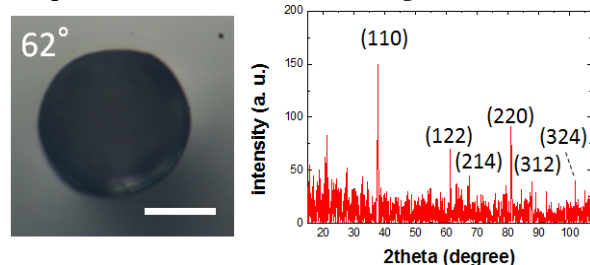
Fig. 8 X-ray analysis showing the cross-sectional shape is almost circular. Crystal planes of (110), (220), (312), (122), (214), (324) incline 0, 0, 10, 13, 16, 25 degrees for c-axis.

Fig. 8 shows that a resonator consisting of crystal planes inclining about 30 degrees has a circular cross-sectional shape.

5. Surface etching process

The Q-factor can be improved by reducing surface roughness. The surface roughness of the resonators that we fabricate by crystal growth is 0.35 μm RMS. and this must be improved. We attempted to reduce the surface roughness with etching. Etching makes the cavity shape polygonal thanks to the crystalline material. However, we can fabricate a circular shape by changing the seed rod angle despite the effect of the crystal. So we think that etching can reduce the surface roughness while maintaining a circular shape.

The 3:1 $H_2SO_4 : H_3PO_4$ mixture is the routinely employed chemical treatment for sapphire preparation. And we used the mixture at 260 ℃ for 3 hours. Fig. 9 shows the surface of the resonator before and after etching as observed with a laser microscope.
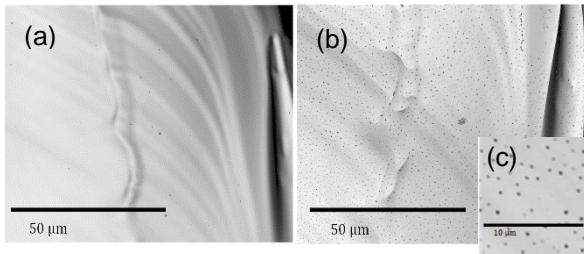

Fig. 9 Laser microscope image of resonator surface.
(a) Before etching. RMS roughness is 0.35 μm
(b) After etching. RMS roughness is 1.88μm
(c) After etching. Enlarged image of Fig. 9 (b).

We found that etching worsened the surface roughness. This is because etching emphasizes the irregularity of the surface. However, the surface when we observe the surface of a narrow part may be smooth.

Fig. 9 (c) is an enlargement of Fig. 9 (b) that reveals many holes in the surface. Etching with phosphoric acid forms holes when there are defects in the crystal structure. So a resonator fabricated by crystal growth has some defects in its crystal structure, and it is thought that these defects lead to the low Q-factor caused by surface roughness.

6. Conclusion

We analyzed the theory behind the fabrication of a circular cavity. And we were able to change the cross-sectional shape of the microcavities from a polygon to a circle by changing the angle of the seed rod. In the future we will improve the crystal growth method to reduce the number of surface defects.

References

[1] A. Yokoo, S. Tomaru, I. Yokohama, H. Itoh, and T. Kaino, "A new growth method for long rod like organic nonlinear optical crystals with phase-matched direction," J. Cryst. Growth **156** 279-284 (1995).

[2] H. Kudo, Y. Ogawa, A. Yokoo, and T. Tanabe, "Fabrication of whispering gallery mode cavity using crystal growth," Appl. Phys. Lett., **102**, 211105 (2013).

[3] H. Kudo, R. Suzuki, and T. Tanabe, "Whispering gallery modes in hexagonal microcavities," Phys. Rev. **88**, 023807 (2013).

[4] Elena R. Dobrovinskaya, Sapphire: Material, Manufacturing, Applications, (Springer, 2009).

Design of a fiber Fabry-Perot cavity for optimized coupling to an optical fiber

Yohei Ogawa (M2)

Quantum information processing requires low-loss coupling between optical fiber and a microcavity. In 2010, a fiber Fabry-Perot cavity (FFPC) was proposed that stores photons between fiber mirrors in air. This FFPC is said to have good coupling efficiency. However, the observed power-coupling rate differs from the rate calculated using the approximation formula. I directly calculate the electro-magnetic field in the FFPC structure with the finite-difference time domain (FDTD) method. I show that the Bragg mirror causes a large loss, and I present a possible way of avoiding this loss.

Key words: Microcavity, Fabry-Perot cavity, cavity QED, Bragg mirror, FDTD calculation

1. Introduction

In recent years, research dealing with the interaction between light and atoms, known as cavity quantum-electro-dynamics (QED), has attracted a lot of interest. Photons and materials with two energy levels, i.e. atoms, couple together in an optical microcavity. The atoms are then excited and emit the photons as a result of natural relaxation. Photons naturally move away from atoms, but they can be coupled with atoms in a microcavity. When we employ the coupling rate between photons and atoms g, the relaxation from atoms to the outside γ, the relaxation from the cavity to the outside κ, we call the state $g < \gamma, \kappa$ weak coupling and the state $g > \gamma, \kappa$ strong coupling. The goal of cavity QED research is to achieve quantum transmission with strong coupling.

Researchers have used solid microcavities to perform experiments related to cavity QED. It caused weak coupling and two-level materials could not exist anywhere in the light field. On the other hand, the Fabry-Perot cavity (FPC), which stores light in air, has a large cavity volume and making it smaller is too expensive. For these reasons, cavity QED researchers have tended to ignore FPCs.

Therefore, the fiber Fabry-Perot cavity (FFPC) was developed by Hunger et al. in 2010 [1]. They process the optical fiber surface with a CO_2 laser, form a dielectric mirror and arrange two fibers so that they face each other. This method does not need an optical waveguide to introduce the photons and the cavity volume can be very small. However, Hunger's group reported that the calculated power-coupling rate is about 97% while the experimentally observed rate is 85%. In this report, I directly calculate the electro-magnetic field with the finite-difference time domain (FDTD) method in the FFPC structure and discover that a dielectric Bragg mirror designed for a single wavelength causes a large optical coupling loss.

2. FFPC design

The FFPC structure is shown in Fig. 1 (a). The critical FFPC values are the mirror curvature R and mirror distance L. The beam spot size at the center w_0 and on the mirror w_1 are calculated with eq. (1) and (2).

$$\omega_0 \approx \sqrt{\frac{\lambda}{\pi}} \left(L \frac{R_1 R_2}{R_1 + R_2} \right)^{\frac{1}{4}} \qquad (1)$$

$$\omega_1 = \sqrt{\frac{2L}{k} \frac{1}{\sqrt{\left(2 - \frac{L}{R}\right)\frac{L}{R}}}} \qquad (2)$$

I show the relation between ω_1 and L in Fig. 1 (b) based on eq. (2). In this report, since the core diameter of the optical fiber is about 10 μm, I decided to use $R = 100$ μm, $L = 40$ μm to obtain $\omega_1 = 10 \mu m$. These values fulfill the stable conditions requirement of a Fabry-Perot cavity.
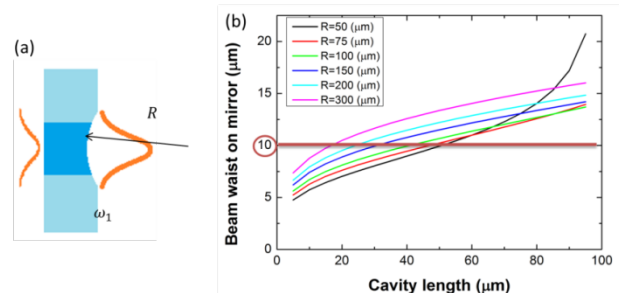

Fig. 1: FFPC parameters. (a) FFPC surface described with mirror curvature R and beam waist ω_1. (b) Relation between ω_1 and L when R is changed.

3. Calculation by FDTD method

With the values decided in section 2, I calculated the electro-magnetic field with the FDTD method. I used Meep 1.2.1 for the FDTD calculation. The FFPC structure is shown in Fig. 2. The mirror formed on the left side is a SiO_2/TiO_2 Bragg mirror $\left(n_{SiO_2} = 1.44, n_{TiO_2} = 2.5, d = \frac{n\lambda}{4}\right)$, while the mirror formed on the right side is a perfect reflection mirror ($n_{metal} = \infty$). The mirror depth is 0.5 μm. I use a $\lambda = 1.55$ μm (normalized frequency $f = 0.645$) light source.

The calculated electro-magnetic field image is shown in Fig. 3 and the field spectrum is shown in Fig. 4. The cavity Q factor is $Q = 9.7 \times 10^4$. With the dielectric mirror, light was inserted in a diagonal direction and passed through the mirror. Here the optical loss is clearly greater than for light coupling from the mirror to the fiber core.
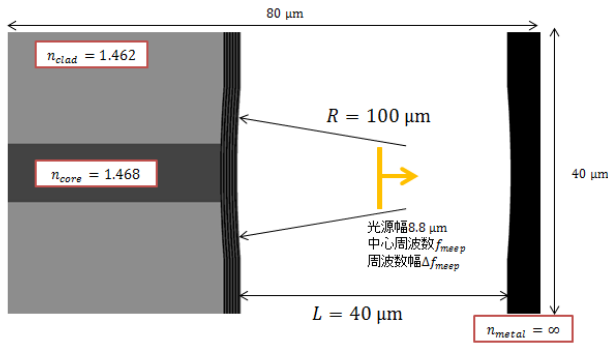

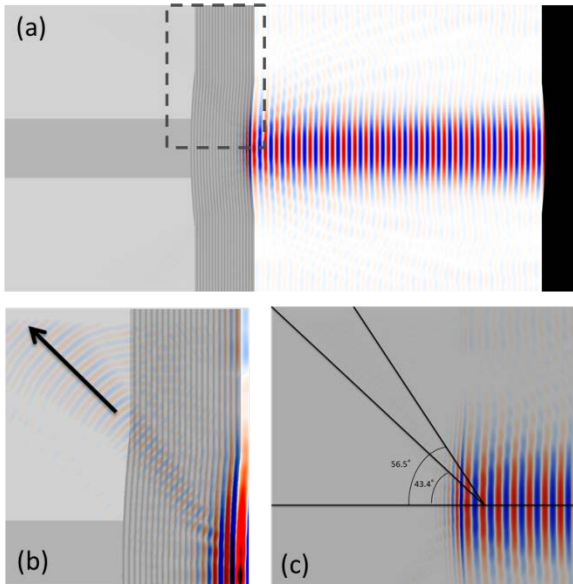Fig. 2: Calculated FFPC structure.

Fig. 3 : Result image showing FFPC structure calculated with FDTD method. (a) Electro-magnetic field in the calculated area. (b) Expanded image near the dielectric mirror. The light passes through the mirror in the wrong direction. (c) Angle measurement from horizontal direction. Light exists between 43.4° ~ 56.5°.

4. Analyze with space Fourier transformation

To determine why the light is transmitted in the wrong direction, I calculate the space Fourier transformation inside the cavity shown in Fig. 3(a). The result is shown in Fig. 5. This image shows that light with a diagonal k vector exists in the cavity because the light diffraction effect is strong in the microcavity and the mirror does not meet the Bragg reflection requirement.

I also consider the requirement for the dielectric SiO_2/TiO_2 mirror. From the size of the photonic band gap, I found that the light angle limitation from the air to the mirror is 54.1°. This approximately equals the angle shown in Fig. 3 (c) so this mirror cannot be used in this situation.
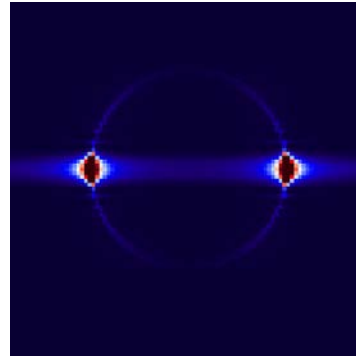
Fig. 5: Image calculated with space Fourier transformation from Fig. 3 (a). Dark red indicates strong light power trapped inside the cavity. The pale blue circle indicates light with a diagonal k vector.

5. Conclusion

In this research, I analyzed the FFPC structure with the FDTD method and found that there is leakage from the Bragg mirror, which has not previously been considered. This is a serious problem when the cavity is very small. We might solve it by using a specialized mirror that takes account of the mode profile design, as often used in photonic crystal microcavities.

References

[1] D. Hunger *et al.*, *New J. Phys.* **12**, 065038 (2010)
[2] T. Tanabe *et al.*, *The Review of Laser Engineering* **45**, 575 (2012)

Fast algorithm for obtaining theoretical quality factor of two-dimensional photonic crystal cavity using mode profile

Akihiro Fushimi (M1)

We need to use the three-dimensional finite-difference time-domain method to obtain the Q of a photonic crystal nanocavity. However, we need to calculate the total energy at every step to obtain an accurate Q, and this requires a large calculation cost. Here we study a method that can acquire the Q of a two-dimensional photonic crystal nanocavity from a two-dimensional mode profile at the center of a photonic crystal slab without the need for a costly three-dimensional energy calculation. As a result, we can greatly shorten the calculation time.

1. Introduction

Today, we are becoming aware of the limitations of electronic devices. In contrast, photonic technology is attracting attention as a possible way of breaking through these limitations. Photonic crystal (PhC) nanocavities [1,2] are made by using semiconductor processes, and can be mounted on a Si slab because of their μm order size. So, the PhC nanocavity is regarded as a potential device for trapping and controlling light.

When we design a PhC nanocavity, we usually use three-dimensional finite-difference time-domain (3DFDTD) simulations. For this analysis, we obtain important cavity parameters including its resonant wavelength, and quality factor (Q). However, 3DFDTD consumes a lot of computational resources. Fortunately, we can parallelize the FDTD code, and so we can accelerate the calculation by using a parallel computer and graphics processing unit (GPU), which has many cores. In particular, GPU performance is improving greatly and the GPU price is low. To obtain the Q factor of a cavity accurately, we need to calculate the total energy in the calculation area every calculation step. This calculation is difficult for a GPU to accomplish because it is poor at sequential computation, and so the required FDTD time becomes very long.

We propose a new method that obtains a Q factor by using a 2D mode profile in the center of a PhC slab rather than a 3D energy calculation. Furthermore, our method can employ the mode profile as soon as the light sources finish their excitation, and we obtain the Q factor even if the calculation area is small. Therefore, this method greatly reduces the calculation time.

2. Algorithm

The radiation losses of 2DPhC microcavities are the primary factor limiting the Q factor. We obtain the in-plane momentum components $|k_{//}|$ by using the spatial Fourier transformation of the mode profile in a cavity. The momentum components k in a slab whose refractive index is n is given as

$$k^2 = k_\parallel^2 + k_\perp^2 = \left(\frac{n\omega_0}{c}\right)^2 \tag{1}$$

where $k_{//}$ represents the vertical momentum components, ω_0 is the angular frequency of light, and c is the speed of light. The angle incident to the face of slab φ_1 is given as

$$\varphi_1 = \tan^{-1}\left(\frac{k_\parallel}{k_\perp}\right) \tag{2}$$

When $|k_{//}|$ lies within the range

$$k_\parallel < \frac{\omega_0}{c} = k_0 \tag{3}$$

the wave escapes to the air cladding because the light cannot satisfy the total reflection condition. This region is referred to as the light cone (LC) [3]. We improved the Q factor by following the design principle that we need to reduce the number of the components in the LC [4,5]. However, there has been no evaluation study of the relation between LC components and Q factor.

Our method estimates the loss rate by weighting each radiation mode component according to transmittance and the number of transmittances per second. First, the angle of refraction φ_2 is given as

$$\varphi_2 = \sin^{-1}(n \sin\varphi_1) \tag{4}$$

provided that we establish a vacuum around the slab. A PhC microcavity is usually coupled with a TE-like mode, so the amplitude transmittance t_s is given as

$$t_s = \frac{2n\cos\varphi_1}{n\cos\varphi_1 + \cos\varphi_2} \tag{5}$$

Energy transmittance T_s is given as

$$T_s = \frac{\cos\varphi_2}{n\cos\varphi_1}|t_s|^2 \tag{6}$$

When thickness of the slab is d, the number of reflections per unit time N is given as

$$N = \frac{c}{nd}\cos\varphi_1 \tag{7}$$

The energy in the cavity U is equal to the sum of each energy of TE mode's Ex, Ez, and Hy.

$$U = U_{E_x} + U_{E_z} + U_{H_y} \quad (8)$$

The Q factor is defined as

$$Q = \omega_0 \frac{U}{\left|\frac{dU}{dt}\right|} \quad (9)$$

Our method uses a 2D mode profile when the energy is concentrated only in electric fields Ex and Ez.

$$U_{E_x} + U_{E_z} = U, \qquad U_{H_y} = 0 \quad (10)$$

We can get loss rate L_{Ex} and L_{Ez} by weighting of each of LC components according to transmittance and the number of transmittance per second. From Eqs. (8)~(10), Q-factor is given as

$$Q = \omega_0 \frac{U_{E_x} + U_{E_z}}{U_{E_x} L_{E_x} + U_{E_z} L_{E_z}} \quad (11)$$

From Eqs. (6) and (7), the loss rate is given as

$$L = \iint_{LC} |E(k)|^2 \cdot T_s \cdot N \, dk \quad (12)$$

We use the effective refractive index neff of each element as refractive index n in the slab. neff is given as

$$n_{\text{eff}} = \frac{\iint_{\text{all}} k \cdot |E(k)|^2 \, dk}{k_0 \cdot \iint_{\text{all}} |E(k)|^2 dk} \quad (13)$$

We approximate U_{Ex} and U_{Ez} with the following equation.

$$U_E = \iint_{\text{all}} |E(k)|^2 dk \quad (14)$$

Equation (14) does not take account of the refractive index in real space because this equation means the summation in momentum space. However, we consider this problem by using the effective refractive index.

3. Results

First, we apply our method to an L3 resonator [4]. The design is shown in Fig. 1. The lattice constant a is 420 nm, the air holes radius r is 115.5 nm, and the slab thickness d is 210 nm. The air holes in the side of resonator are shifted 32 nm from their original position, and their radius is 63 nm. The xy plane, which passes through the center of the resonator, is a symmetry plane. The resonance wavelength is 1572 nm. The FWHM of the light source is about 3 nm. The spatial and momentum mode profiles are shown in Fig. 2. Fig. 3 shows the Q factor obtained by the conventional method. Namely, it is calculated by decreasing the energy in the calculation area and applying our method. We apply our method when the light has just stopped, after 250 fs, and after 1 ps. The number of layers means the number of the rows

between the resonator and the boundary of the calculation area.

When there are very few layers, the previous method normally estimates a lower Q factor because the horizontal leak increases, and the energy moves outside the calculation area, so the loss rate is larger. On the other hand, our method makes it possible to obtain the "true Q factor" that it is the Q factor when the number of layers is infinity. Fig. 3 shows the number of layers versus the Q factor of the L3 resonator.

So, we can shorten the calculation time by reducing the calculation area. Furthermore, we obtained a similar Q factor when using the mode profile at different times (just as the light stopped, after 250 fs, and after 1 ps). This result shows we can obtain the Q factor accurately even if we continue to calculate until the light stop as long as we set the light adequately. The conventional method requires us to continue calculating for a few ps after the light has stopped, but our method does not, so we can again shorten the calculation time.
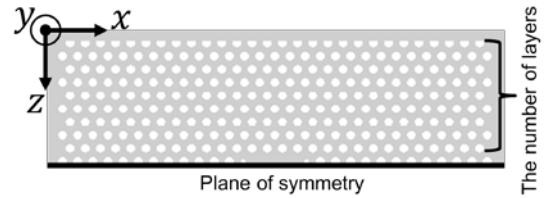
Fig. 1: The design of L3 resonator.
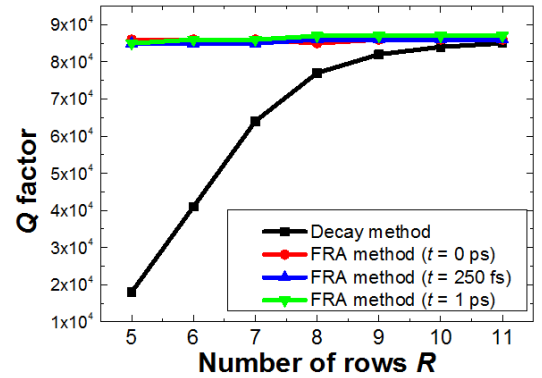
Fig. 2: The mode of the L3 resonator. The top figures show the spatial mode profile, and the bottom figures show the momentum mode profile.

Next, we apply our method to a width-modulated line defect nanocavity [6]. This design shows Fig. 4. Lattice constant a is 420 nm, radii of air holes r is 108 nm, and thickness of the slab d is 205 nm. The shift of the air holes in the side of the resonator is 9-6-3 nm from their original position following. The plane of xy, which passes through the center of the resonator, is a symmetry plane. This resonance wavelength is 1568 nm. The light source's FWHM is about 0.8 nm. The spatial and momentum mode profile shows Fig. 5. Q-factor getting by the usual method that calculates by decreasing the energy in the

calculation area and our method show Fig. 6.

Figure 6 shows Q-factor getting by two method is difficult when the number of the layer is 11, but Decay's value asymptote the value getting by our method, so when the number of the layer is larger, it is expected that the usual method's Q-factor is similar to our method's one.

Fig. 3: The number of layers versus the Q factor of the L3 resonator.

Fig. 4: The design of width-modulated line defect nanocavity.

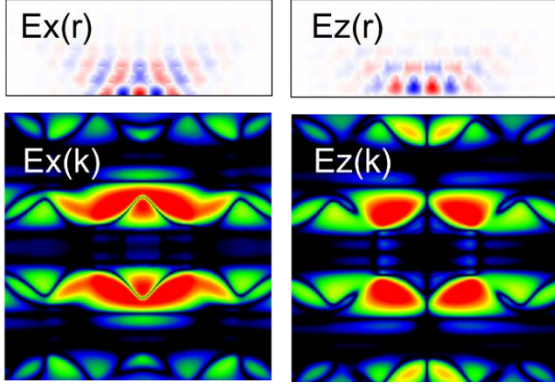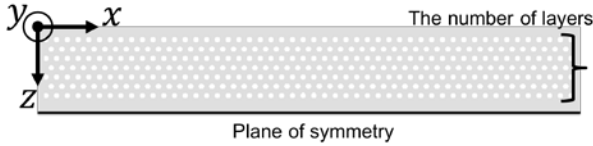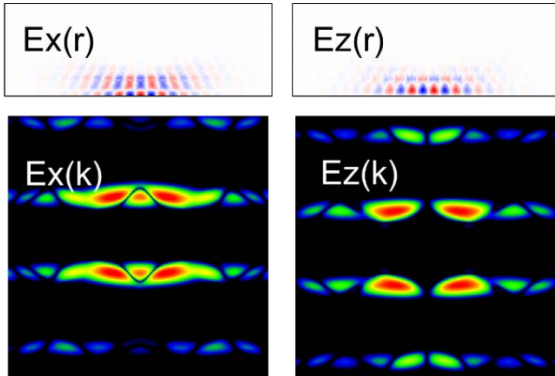Fig. 5: The mode of width-modulated line defect nanocavity. The top figures show the spatial mode profile, and the bottom figures show the momentum mode profile.

4. Calculation time

Finally, we show how we can reduce the calculation time. We perform a comparison using an L3 resonator and a width-modulated line defect nanocavity. We define the time required for the conventional method to be the calculation time until 1.25 ps after the light stops with energy calculated every step when there are 11 layers. The time required for our method is calculation time until the light stops without calculating energy when there are 5 layers. This result is shown in Fig. 7. Provided that we define this
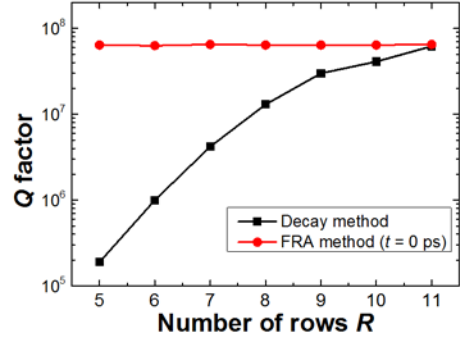
Fig. 6: The number of layers versus the Q factor of a width-modulated line defect nanocavity.

calculation time as (practical time)×(the number of nodes), by using our method, we can shorten the calculation time by 1/4.2 with a L3 resonator, and surprisingly by 1/5.2 with a width-modulated line defect nanocavity.
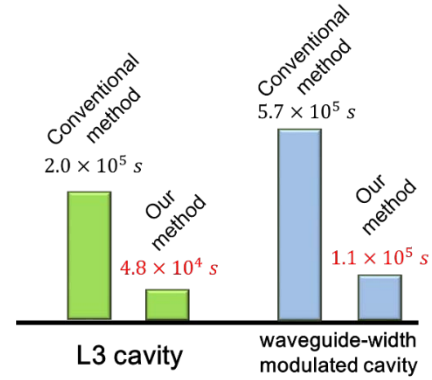
Fig. 7: Reduction of calculation time.

5. Summary

We propose a new method that obtains the Q factor of a 2D PhC resonator by only a 2D mode profile at the center of a PhC slab. Our method can use the mode profile immediately after the excitation of the light source has finished, and we obtain the Q factor even if the calculation area is smaller. Therefore, this method greatly shortens the calculation time. This method allows the more efficient use of computer resources, and with an optimization algorithm, we can look for a higher Q-factor resonator.

References

[1] E. Yablonovitch, Phys. Rev. Lett. **58**, 20, 2059-2062 (1987).
[2] K. Nozaki, *et al.*, Opt. Express **21**, 10, 11877-11888 (2013).
[3] K. Srinivasan and O. Painter, Opt. Express **10**, 15, 670-684 (2002).
[4] Y. Akahane, *et al.*, Nature **425**, 944-947 (2003).
[5] Q. Quan and M. Loncar, Opt. Express **19**, 19, 18529-18542 (2011).
[6] Kuramochi, *et al.*, Appl. Phys. Lett. **88**, 041112 (2006).

Evaluation of characteristic and fabrication variance of silicon photonics devices produced by CMOS

Shohei Tomiyama (B4)   Akihiro Fushimi (M1)

We produced 30 chips on which silicon photonics devices were integrated at the Institute of Microelectronics (IME), and measured the resonant wavelengths and Q factors of 24 chips. We compared the fabrication variance of silicon photonic devices with the results of previous research undertaken at our laboratory. In addition, we recorded a Q factor of 1.6×10^5, which is the highest value yet reported as a width-modulated line defect photonic crystal nanocavity manufactured by the CMOS process.

Key words: Silicon photonics, Optical integrated circuit, CMOS process, width-modulated line defect photonic crystal nanocavity, Silicon microring resonator.

1. Introduction

In the 21st century, silicon photonics continues to develop rapidly. In recent years the environment that enables us to manufacture silicon photonic devices by the CMOS process has been well regulated. Electron beam lithography has been mainly used to produce silicon photonics devices, but for individual researchers it had been difficult to manufacture silicon photonics devices using CMOS. However, in the last few years, CMOS foundries such as the Institute of Microelectronics (IME) have emerged, thereby enabling the low-cost manufacture of large-scale systems by CMOS [1]. We designed a chip on which silicon photonics devices are integrated and fabricated 30 such chips at IME.

According to our previous research, it is necessary to reduce any fabrication variance to less than the width of the resonant spectrum of microring resonators so that an all-optical logic gate constructed with microring resonators definitely works [2].

We measured the Q factors and resonant wavelengths of 24 sample microring resonators and width-modulated line defect photonic crystal nanocavities. We compared the fabrication variance of the microring resonators with the results of our previous research.

2. Construction of measurement system

Fig. 1 shows our measurement system. We constructed experimental equipment to evaluate the characteristics of silicon photonic devices. The measuring modules were fixed on piezo stages that work with a precision of 1 μm and in the range of 4 mm at maximum. The stage can move vertically and along the depth in fig. 1.
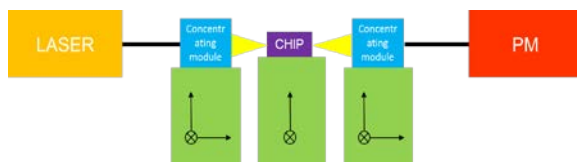

Fig. 1: Diagram of measurement system.

We installed an IR camera and a visible light camera to observe a chip from above. The visible light camera is used to roughly adjust the position of a module of interest and a waveguide on the chip. We use the IR camera to perform fine adjustments so that light is incident more exactly on the waveguide.

Dimension of the chips are 8×2 mm. A chip consists of silicon substrate, silica under cladding, silicon slab and silica over cladding. The devices we designed are fabricated in the silicon slab layer whose thickness is 210 nm. Silicon wire waveguides which is for putting light into/out devices extend from one end to another and they have spot size converters (SSCs) at each ends. They are set in columns every 50 μm and the number of them are 150. Figure 2 shows the photographs of microring resonators and width-modulated photonic crystal nanocavities. The diameter of the microrings, the width os silicon wire waveguides and the gap distance between waveguides and microrings are 10 μm, 400 μm and 200 μm, respectively.
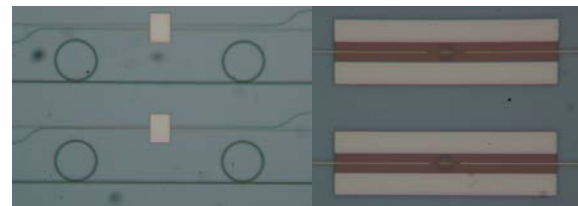
Fig. 2: Microring resonators and width-modulated line defect photonic crystal nanocavities.

3. Measurement of transmission spectrum

We measured the transmission spectra of 24 silicon microring resonators and the same number of width-modulated line defect photonic crystal nanocavities. The input power was -15 dBm and the wavelength was swept from 1500 to 1630 nm. A preliminary experiment showed that the loss of the silicon waveguide was -7 dB/cm or less and that of the SSC was not more than -1.5 dB on one side.

Fig. 3 shows one of the transmission spectra that we measured. We used the resonant spectrum of the microring resonator shown with a red arrow to determine the Q factor and the resonant wavelength. The photographs in Fig. 3 caught the moment of resonance.
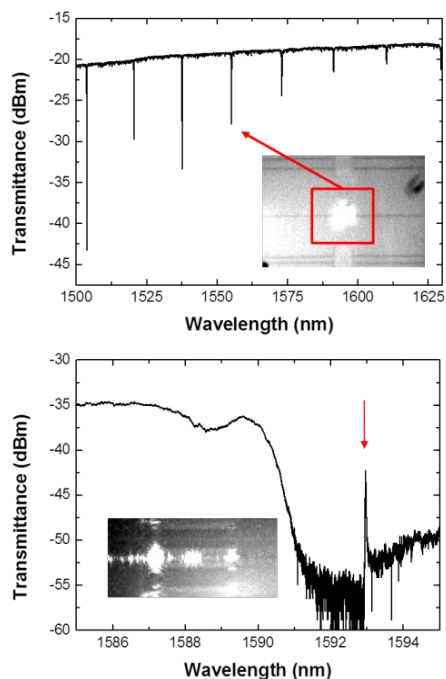
Fig. 3: Transmission spectra of a microring resonator (top) and a width-modulated line defect photonic crystal nanocavity (bottom). The photographs caught the moment of resonance

The highest Q of a microring resonator was 2.0×10^4 and that of a width-modulated line defect cavity was $Q = 1.6 \times 10^5$. The highest Q of a width-modulated line defect cavity was also the highest value yet reported for such a cavity fabricated by the CMOS process. The highest Q of a width-modulated line defect cavity manufactured by electron beam lithography is about ten to the power of six, thus showing the difference in precision between width-modulated line defect cavities manufactured by CMOS and those manufactured by electron beam lithography.

4. Evaluation of fabrication variance

Table 1 shows the average value and standard deviation of the resonance wavelength and the Q level of each resonator. Fig. 4 shows the corresponding histograms.

Table 1: Statistics of the resonant wavelengths and Q factor

Silicon microring resonator	Resonant wavelength (nm)	Q factor
Average	1550.9	1.3×10^4
Standard deviation	4.9	0.3×10^4
Photonic crystal	Resonant wavelength (nm)	Q factor
Average	1587.6	8.1×10^4
Standard deviation	7.6	3.8×10^4
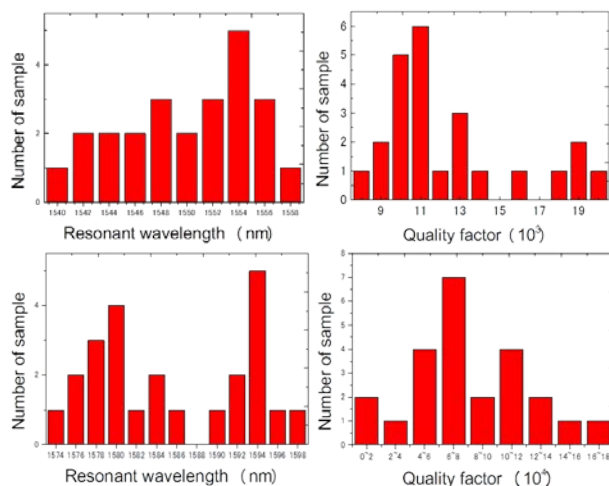
Fig. 4: Top: Histograms of the resonant wavelengths (left) and Q factors (right) of microring resonators. Bottom: Histograms of the resonant wavelengths (left) and Q factors (right) of width-modulated line defect photonic crystal nanocavities.

According to the above-mentioned previous study, an all-optical logic gate constructed with microring resonators will definitely perform satisfactorily if the fabrication variance of the microring resonators is less than their resonant spectrum width.

We calculated the width of the resonant spectrum from the Q factor. A comparison revealed that it is necessary to reduce the fabrication variance to several percent or less.

5. Conclusion

In this study, we measured the resonant wavelengths and Q factors of silicon microring resonators and width-modulated photonic crystal nanocavities fabricated by CMOS, and we compared the fabrication variance of the microring resonators with the result of our previous study. As a result, we revealed that to reduce the fabrication variance to several percent or less we must construct the all-optical logic gate with microring resonators whose performance is guaranteed. In addition, we measured $Q = 1.6 \times 10^5$, which is the highest Q factor yet reported for a width-modulated photonic crystal nanocavity manufactured by CMOS.

References

[1] T, Baba, IEICE **94**, 12, 1037-1040 (2011).
[2] A. Fushimi and T. Tanabe, Opt. Exp. **22**, 4, 4466-4479 (2014).

Robustness of scalable all-optical NAND gate

Akihiro Fushimi (M1)

We designed scalable all-optical logic gates based on microrings that operate at the same input and output wavelengths.   We investigated the influence of input power fluctuations and fabrication errors.

1. Introduction

Recent progress on ultrahigh-Q microcavities has enabled us to develop an all-optical logic gate on a chip that operates at ultralow power [1]. Several groups have demonstrated logic operations numerically [1], but experimental implementation has remained a challenge. There are certain criteria that a system must satisfy. First, the input and output signals must have the same wavelength; otherwise it is extremely difficult to connect systems in tandem.   Secondly, it is preferable to construct the system with one cavity design, because the fabrication will then be easier. Although we can use an ideal structure in a simulation, in practice there are fabrication errors and power fluctuations.

2. Basic elements of logic gates

We use silicon nitride (Si3N4) microring resonators because they can employ the optical Kerr effect thanks to the large bandgap of the material.   The cross-section of the air-clad waveguide is 900 nm wide and 600 nm high. Figure 2 is a schematic illustration of the microcavity. The radius of the ring resonator R is 20 μm; hence the mode volume V of the cavity is 1.5×10^2 μm3.   The linear and nonlinear refractive indexes are $n_0 = 1.98$, and $n_2 = 2.5 \times 10^{-15}$ cm2W-1, respectively.   We assume the cavity resonates at 1550 and 1580 nm.   The unloaded quality factor (Q_{unload}) for both resonant modes is 1.0×10^6, and this value is given by $Q = \omega_0 \tau_{loss}$, where ω_0 is the resonant angular frequency of the cavity and τ_{loss} is the loss rate towards the outside.   The input wavelengths are slightly detuned from the resonance and are set at $\lambda_1 = 1550.01$ nm and $\lambda_2 = 1550.02$ nm.

wavelength is used as a signal and the other as a control. Throughout this study, we use coupled mode theory (CMT) [2] to analyze the logic gate operations.

3. Designs of all-optical logic circuits

First we design a NAND gate, since it is a basic element of logic gates. The photonic circuit is shown in Fig. 2(a), and is made of five cavities denoted C1, C2, C3, C4, and C5, which had τ_{coup} values set at 150, 100, 250, 250, and 100 ps, respectively.   C1 and C3 switch the signals on and off, and thus contribute directly to the logic operation.   C4 is used to switch between λ_2 and λ_1. C2 and C5 are used to filter out unnecessary drive light.
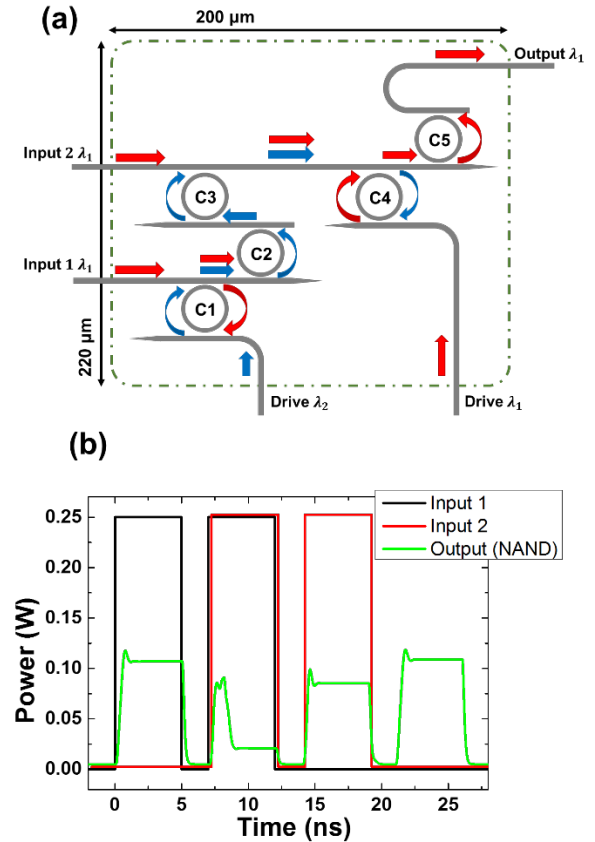
Fig. 2:   (a) Design of all-optical NAND gate based on microring cavities.   (b) Input and output versus time. The black, red, and green lines represent input 1, input 2, and output, respectively.

Input 1, input 2 and the output signals are at the same wavelength λ_1.   We use two different

Fig. 1:   Operating principle of Kerr switching.

Figure 1 shows an example switching operation in an add-drop ring resonator system, where one

wavelengths to drive the system; but as discussed previously, this does not degrade system scalability. Pulsed drive sources with an amplitude of 360 mW are applied with a cycle of 5 ns and a duty ratio of 60%.

Figure 2(b) shows the calculated output waveform when inputs 1 and 2 are applied as shown in the graph. First, we set high input 1 (ON) and low input 2 (OFF) from 0 to 3 ns. The output exhibits a high state. When we switch both inputs to a high state (from 5 to 8 ns), the output is in a low state. We obtained a low state only when inputs 1 and 2 are both high, and this corresponds to a NAND gate operation.

4. Input power fluctuations

We investigated the system tolerance to input power fluctuations by calculating the output amplitude with different input powers. We set the drive light power at 360 mW, and changed the amplitude of the input signal. Figure 3 shows the input and output characteristics for four different gates. The black square dots show when we set the powers of inputs 1 and 2 at the same value and changed both powers simultaneously. The red circular dots indicate the output amplitude when we fixed the input 2 amplitude at 250 mW and changed input 1. The blue triangles show the result we obtained when we fixed input 1 at 250 mW and changed the power of input 2.

Figure 3(a) and (b) show the output amplitudes for AND and OR gates. The output of an AND gate is at a low state when one of the inputs (1 or 2) is less than 60 mW. The output signal rises when the input exceeds 100 mW. The output is unstable when the input is between 60 and 100 mW. When we set the output power threshold at 50 mW, we need an input larger than 170 mW. However, if we increase the input too much, the output amplitude decreases again. This is due to the supply of excess λ_2 light to the C4 cavity of the AND gate. This analysis reveals that the optimized input is in the 160 to 300 mW range for a high input and from 0 to 50 mW for a low input. This tolerable power range is sufficiently large for practical use.

Figure 3(c) shows the NOR gate output. The output is low only when inputs 1 and 2 are both at a low state. The graph shows that this gate is at a low state when both inputs are less than 80 mW. When the input increases to 300 mW, the output amplitude rises. As a result of this analysis, we found that the input power for this NOR gate must set in the 60 to 300 mW range for a low input.

Figure 3(d) shows the NAND gate output. The output is low only when inputs 1 and 2 are both at a high state. The graph shows that the system exhibits a low output when the input power exceeds 230 mW. When the input increases to 400 mW, the output amplitude rises. As a result of

this analysis, we found that the input power for this NAND gate must set in the 230 to 400 mW range for a high input and at less than 50 mW for a low input.

The results for all the gates show that the upper limit of the OFF signal is 40 mW and is restricted by the OR gate, and the lower limit of the ON signal is 230 mW and is restricted by the NAND gate, when we set the output threshold value at 50 mW. Through this study, we found that the input power fluctuations are not a critical issue in our system.
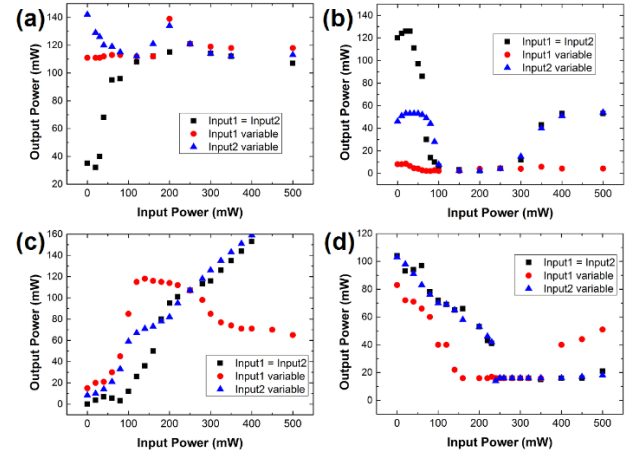

Fig. 3: Input and output amplitudes of different logic gates versus time. (a) AND gate. (b) OR gate. (c) NOR gate. (d) NAND gate. The black squares are the output when the power of inputs 1 and 2 were changed together, the red circles are the output when only input 1 was changed (input 2 is fixed at 250 mW). The blue triangles are the output when only input 2 was changed (input 1 is fixed at 250 mW).

5. Resonant wavelength fluctuations

Next, we investigated the effect of the resonant wavelength fluctuation of cavities. Resonant wavelength fluctuations occur as a result of imperfect fabrication. Our system uses 4 (or 5) cavities, and each cavity has two resonant modes. To investigate the effect of the presence of wavelength fluctuation, we added random fluctuations to all the 8 (or 10) resonant modes. Wavelength fluctuations are added based on a normal distribution, and their widths are characterized by standard deviation σ. We calculated the output with CMT, and determined whether or not the system had failed. Table 1 summarizes the result for NAND and other gates. σ_{lim} is the standard deviation that reaches an error rate of 50%. S_{max} is the full width at half maximum (FWHM) of the resonant spectrum of the cavity with the lowest loaded Q used in the system. S_{min} is the FWHM of the spectrum of the cavity with the highest loaded Q used in the system. From the result, we know that the NAND gate is the most sensitive of all types. And the allowed fluctuation is about 0.3 of the cavity width. Although fluctuation where $\sigma < 3.0$ pm is not easy

to achieve, this value can be improved by designing a system where the cavities couple more strongly with the waveguides.

Table 1. Maximum and minimum widths of resonant spectrum (FWHM) S_{max}, S_{min}, and the standard deviation σ_{lim} limit of each logic gate

	OR	NOR	AND	NAND
S_{max}	17.0 pm	17.0 pm	17.0 pm	26.0 pm
S_{min}	8.2 pm	10.0 pm	10.0 pm	10.0 pm
$2\sigma_{lim}$	6.0 pm	4.0 pm	7.0 pm	3.0 pm

6. Gap distance fluctuations

Fabrication error causes both resonant wavelength fluctuations and fluctuations in the cavity-waveguide coupling, because the coupling Q is determined by the gap distance s between the cavity and the waveguide. To simplify this formulation, we assumed that the waveguide width w, refractive index n, and propagation constant β are the same for the cavity and the waveguides. The transverse propagation constant k_x and the evanescent field decay constant a in the cladding are given as

$$k_x = \sqrt{n^2 k^2 - \beta^2} \tag{1}$$

$$\alpha = \sqrt{\beta^2 - n^2 k^2} \tag{2}$$

where k is the wave vector in a vacuum. From Eq. (1) and (2), the mode power P is given as

$$P = \frac{\beta}{2\omega\mu_0}\left(w + \frac{1}{\alpha}\right) \tag{3}$$

where ω is the angular frequency of the light and μ_0 is the vacuum permeability. An expression for the coupling coefficient κ between a straight waveguide and a curved waveguide (microring) is derived as,

$$\kappa = \frac{\omega\varepsilon_0 \cos\left(\frac{k_x w}{2}\right)}{2P(k_x^2 + \alpha^2)}(n^2 - n_0^2) \times \sqrt{\frac{\pi R}{\alpha}}\exp(\alpha s)$$
$$\times \left[\alpha\cos\left(\frac{k_x w}{2}\right)\sinh\left(\frac{\alpha w}{2}\right) \right. \tag{4}$$
$$\left. + k_x\sin\left(\frac{k_x w}{2}\right)\cosh\left(\frac{\alpha w}{2}\right)\right]$$

where ε_0 is the vacuum permittivity. τ_{coup} is given as,

$$\tau_{coup} = \frac{Q}{\omega} = \frac{\pi R n_e}{c\kappa^2} \tag{5}$$

where n_e is the effective refractive index. We need to set the gap distance s at 556, 588, 612, 630, and 644 nm to obtain τ_{coup} of 100, 150, 200, 250, and 300 ps, respectively, and these values are used in our logic gate designs. Now we can directly obtain τ_{coup} from s; hence we can study the impact of the imperfect fabrication of the gap distance s with CMT analysis. In a similar way to that described in the previous section, we added a random error following the normal distribution $\sigma`$ to all of the gaps.

Table 2 summarizes the results for different logic gates. Again the NAND gate is the most sensitive to the error. However, it is possible to achieve fabrication precision of better than ±12 nm with current state-of-the-art fabrication technology.

Table 2. The limit of the fabrication fluctuation (in standard deviation $\sigma`_{lim}$) for different logic gate

	OR	NOR	AND	NAND
$\sigma`_{lim}$	22 nm	25 nm	40 nm	12 nm

7. Summary

We designed all-optical logic gates that operated at the same input and output wavelengths, which makes these logic gates highly scalable and easier to implement in practical use. We demonstrated their operation using coupled mode theory, and investigated various error tolerances. The upper limit of the OFF signal was 40 mW and the lower limit of the ON signal was 200 mW for our logic gate, whose power range is sufficiently robust for practical use. We found that the system was error-free when the device was fabricated with ±5 nm precision and the error rate increased to 50% when the fabrication precision was ±12 nm. In addition, we found that the sensitive dependence on the resonant wavelength fluctuation is critical. The error rate increased to 50% when the resonant wavelength fluctuated 3 pm.

We are attempting to increase the scalability of the system, and this is the first detailed theoretical study of the impact of fabrication error on the operation of such all-optical logic gates, which provides important information that will make it possible to build a bridge between numerical and practical studies.

References

[1] P. Andalib and N. Granpayeh, J. Opt. Soc. Amer. B **26**, 1097 (2009).
[2] J. S. Levy, *et al.*, Nat. Photonics **4**, 37 (2010).
[3] W. Yoshiki and T. Tanabe, J. Opt. Soc. Amer. B **29**, 12, 3335 (2012).

Statistical Data

Publications

(April 2013-March 2014)

Journal Papers:

[1] H. Kudo, Y. Ogawa, T. Kato, A. Yokoo, and T. Tanabe, "Fabrication of whispering gallery mode cavity using crystal growth," Appl. Phys. Lett., Vol. 102, 211105 (pp. 4) (2013).

[2] H. Kudo, R. Suzuki and T. Tanabe, "Whispering gallery modes in hexagonal microcavities," Phys. Rev. A, Vol. 88, 023807 (pp. 7) (2013).

International Conferences:

[1] W. Yoshiki, K. Ishikawa, and T. Tanabe, "Demonstration of wavelength tuning of silica toroid microcavity via additional laser reflow," The European Conference on Lasers and Electro-Optics and the International Quantum Electronics Conference (CLEO®/Europe-IQEC), CK-P.7, München, May 12-16 (2013).

[2] J. Nishimura and T. Tanabe, "Study on Detection of contamination of pure water using silica microsphere," The European Conference on Lasers and Electro-Optics and the International Quantum Electronics Conference (CLEO®/Europe-IQEC), CH-3.3, München, May 12-16 (2013).

[3] H. Kudo, R. Suzuki, A. Yokoo, and T. Tanabe, "High-Q sapphire WGM cavities fabricated by crystal growth," The Conference on Lasers and Electro-Optics (CLEO),CF2I.7, San Jose, June 9-14 (2013).

[4] R. Suzuki, T. Kato, and T. Tanabe, "Octagonal toroid microcavity for mechanically robust coupling with optical fiber", The Conference on Lasers and Electro-Optics (CLEO), JTu4A.44, San Jose, June 9-14 (2013).

[5] H. Kudo, R. Suzuki, T. Kato, A. Yokoo, and T. Tanabe, "Analysis and experimental measurement of the Q factor of hexagonal microcavities fabricated with crystal growth," The 10th Conference on Lasers and Electro-Optics Pacific Rim (CLEO-PR & OECC/PS), WI1-4, Kyoto, June 30-July 4 (2013).

[6] T. Kato, R. Suzuki, and T. Tanabe, "Analysis of Various Whispering Gallery Modes in an Octagonal Silica Toroidal Microcavity," The 10th Conference on Lasers and Electro-Optics Pacific Rim (CLEO-PR & OECC/PS), TuPM-12, Kyoto, June 30-July 4 (2013).

[7] W. Yoshiki and T. Tanabe, "Revealing conditions required for achieving Kerr bistable memory based on whispering gallery mode cavity," 2013 Frontiers in Optics/Laser Science XXIX meeting (FiO/LS), FTu3A.5, Orland, October 6-10 (2013).

[8] A. Fushimi and T. Tanabe, "Exploring high-Q/V mode using optimization algorithm," 2013 Frontiers in Optics/Laser Science XXIX meeting (FiO/LS), FW4E.6, Orland,

October 6-10 (2013).

[9] A. Fushimi and T. Tanabe, "Investigating the robustness of all-optical NAND gates composed by microring cavities," The 3rd International Symposium on Photonics and Electronics Convergence (ISPEC2013), E-5, Tokyo, November 18-10 (2013).

[10]   T. Tetsumoto and T. Tanabe, "Optomechanical waveguide system for switching telecom light," APS March Meeting 2014, H1.00113, Denver, March 3-7 (2014).

Theses

Master Theses

<u>Yohei Ogawa</u> "Design of a fiber Fabry-Perot cavity for an optimized coupling to an optical fiber"

<u>Takumi Kato</u> "Study on the generation of high-order mode-locking in an optical microcavity"

<u>Hiroshi Kudo</u> "Whispering gallery mode microcavities fabricated by crystal growth"

<u>Wataru Yoshiki</u> "Study on an optical switch in a silica toroid microcavity using Kerr effect"

Bachelor Theses

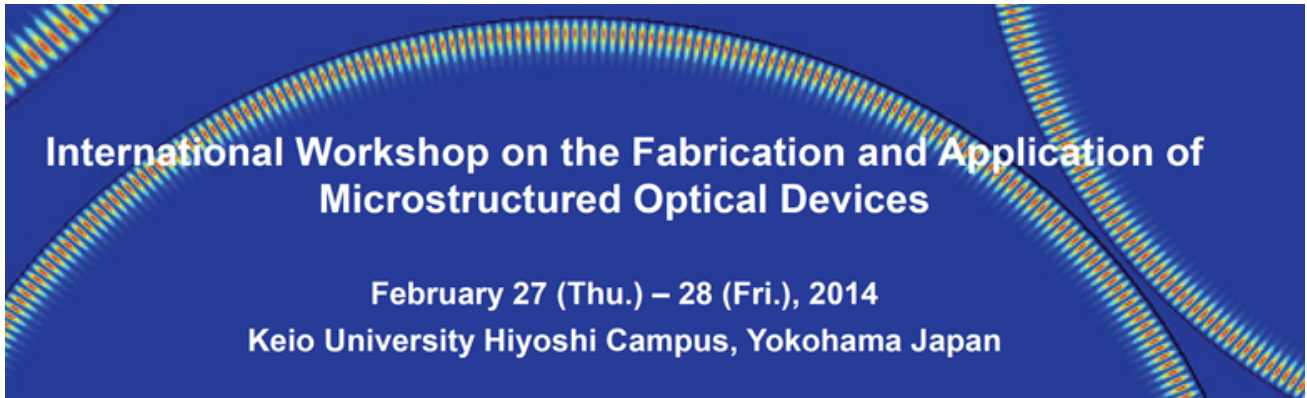<u>Tomoya Kobatake</u> "Feedback control for stable optical Kerr comb generation in a microcavity"

<u>Sho Tamaki</u> "Study on the loss mechanism of a silica toroid microcavity towards the realization of high-Q"

<u>Shohei Tomiyama</u> "Analysis of fabrication error of silicon photonic devices fabricated by CMOS process"

<u>Zhelum Chen</u> "Broadband pulse capture in high-Q cavity using a chirped optical pulse"

<u>Yosuke Nakagawa</u> "Study on the control of the shape and surface processing for higher Q on optical microcavity using crystalline material"

<u>Yui Yakushiji</u> "Multi port input to a whispering gallery mode cavity and its applications"

International Workshop on the Fabrication and Application of Microstructured Optical Devices

February 27 (Thu.) – 28 (Fri.), 2014
Keio University Hiyoshi Campus, Yokohama Japan

We held an international workshop from February 27 to 28, 2015 in Hiyoshi Campus Keio University.　This workshop is intended to provide multidiscipline interaction between precise machining, microstructured optical devices (i.e. microcavities), laser processing, optofluidics, and biomedical applications.　We invited 12 researchers from and outside Japan.

Dr. Toshihiko Baba (Yokohama National University, Japan)

Dr. Eric Chiou (University of California, Los Angeles, USA)

Dr. Tobias Herr (École Polytechnique Fédérale de Lausanne, Switzerland)

Dr. Andreas Klink (Werkzeugmaschinenlabor der RWTH Aachen, Germany)

Dr. Xichun Luo (The University of Strathclyde, UK)

Dr. Lute Maleki (OEwaves Inc., USA)

Dr. Sangkee Min (Lawrence Berkeley National Laboratory, USA)

Dr. Collin Sones (University of Southampton, UK)

Dr. Tatsuya Shoji (Hokkaido University, Japan)

Dr. Frank Vollmer (Max Plank Institute, Germany)

Dr. Andrew Weiner (Purdue University, USA)

Dr. Jiwang Yan (Keio University, Japan)

This conference was sponsored by the Keio University's Program for the Advancement of Next Generation Research Projects.　It was also co-sponsored the Laser Society of Japan.